10

WEAK LENSING AND POLARIZATION

The traditional methods of measuring clustering — angular and redshift surveys — are powerful probes of the power spectrum but share a common deficiency. They are measures of the distribution of galaxies, not the distribution of mass. Theories of the early universe can make very accurate predictions about the latter, but not about the former. A very exciting new technology which probes the mass — not the light — distribution is introduced in this chapter. We will see that the inhomogeneities of the matter induce distortions in the observed shapes of distant galaxies due to gravitational lensing. Further, the statistics of these distortions are directly related to the matter power spectrum.

The anisotropies in the CMB are subject to none of the uncertainties or ambiguities which plague the density field.

- We know exactly where the CMB comes from (the surface of last scattering) so there is no analogue of peculiar velocity distortions.
- There is nothing like the mass vs light problem which afflicts the interpretation of galaxy surveys.
- In addition, the mass distribution has gone nonlinear, so a simple comparison of the linear power spectrum derived in Chapter 7 with the data is dangerous. Anisotropies in the CMB are still at the part-in-a-hundred-thousand level, so nonlinearities are for the most part irrelevant.

The C_l's then are easy to interpret and extract information from. Nonetheless, here too we can go beyond what we have already done. Until now we have focused on anisotropies in the temperature field. Compton scattering before decoupling also induced polarization anisotropies. Polarization opens up a new dimension in the study of the CMB. At the very least, it doubles the amount of information contained in the CMB. As we will see in this chapter, the promise of polarization goes well beyond this doubling. Gravity waves — tensor perturbations — produce a particular pattern of polarization that cannot be mimicked by scalar perturbations. Therefore, polarization offers a unique way of searching for gravity waves produced during inflation.

Gravitational lensing and polarization belong in the same chapter primarily because the mathematics describing them is so similar. Both effects can be quantified with a two-by-two symmetric matrix. In lensing, this matrix is the *distortion tensor* encoding information about image distortion. The polarization tensor has a longer history with more famous components Q and U. It is identical mathematically, though. So, the technologies used to study both of these effects are very similar.

10.1 GRAVITATIONAL DISTORTION OF IMAGES

The cosmological gravitational field distorts the paths traveled by light from distant sources to us. This fundamental fact carries with it an enormous amount of cosmological promise. Most important is the idea that light paths respond to *mass*. If we can measure distortions, then, we might be able to infer something about the distribution of mass in the universe. The importance of this inference cannot be overstated: most of what we think we know about this distribution comes from our observations of the galaxy distribution. We hope that, on large scales at least, the two — the mass and the galaxy distribution — are not too different. If we observe the mass distribution directly via distortion of light rays, though, then we need not rely on this hope. We can then directly compare observations with theoretical predictions. For cosmology, therefore, we expect the most important aspect of light ray distortion to be *weak lensing*, wherein the shapes of distant galaxies are distorted (slightly) by intervening foreground mass overdensities. We begin with an overview of image distortion along with a brief discussion of some other applications.

The idea that gravitational fields might distort distant images is as old as general relativity. Indeed, even before Einstein finalized general relativity, he understood the importance of measuring this distortion. Early notebooks of his contain calculations of the magnification of images and of the possibility of a double image of a single source (Renn, Sauer, and Stachel, 1997). And it was detection of gravitational distortion that led to the acceptance of general relativity. In 1919, Eddington led a voyage to the Southern Hemisphere to observe the deflection of starlight during a solar eclipse. The magnitude of this effect (Dyson, Eddington, and Davidson, 1920) was in good agreement with Einstein's new theory.

One of the most spectacular manifestations of gravity bending light paths is strong gravitational lensing. In 1979, Walsh, Carswell, and Weymann observed a multiply imaged quasar, thereby confirming Einstein's early speculations. Light rays leaving the quasar in different directions are focused on the same point (us) by an intervening galaxy. Since then, dozens of multiply imaged quasars have been observed, and we are on the verge of discovering many hundred more in the near future. Exactly what fraction of quasars is lensed is a question that may depend on the background cosmology. In particular, it has been argued that there should be more multiply imaged quasars in a universe with a cosmological constant than in one without (see Exercise 1 and Kochanek, 1996).

There are other examples of gravitational lensing that have an impact on cosmology. Light rays that take different routes to the same endpoint typically arrive at that endpoint at different times. Therefore, two light rays emitted from the same source at the same time which we detect from different directions due to lensing typically arrive at different times. We can measure this time delay by studying sources with variable emission. The delay turns out generally to depend on the Hubble constant, so astronomers have made very accurate measures of H_0 looking for time delays (e.g., Kundic *et al.*, 1997). Another example is microlensing, wherein a lens moves into the line connecting a source to us. When it does, the image is magnified, so that we observe a characteristic variability in the distant source. Microlensing has been used in recent years to find massive compact halo objects (MACHOs) in our galaxy (Alcock *et al.*, 1993). It now appears that MACHOs do not make up all, or even most, of the dark matter in our galaxy. Nonetheless, exactly what and where they are is still a mystery of cosmic significance.

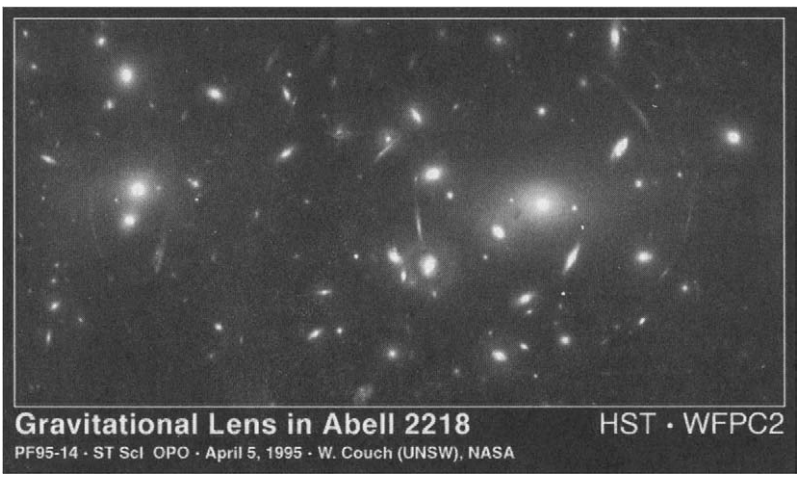

Figure 10.1. Foreground galaxies in the cluster Abell 2218 distort the images of background galaxies. Elliptical arcs surround the central region of the cluster at right.

Yet another spectacular manifestation of gravitational lensing is shown in Figure 10.1. The large cluster in the foreground, Abell 2218, distorts the shapes of the background galaxies. This leads to a distinctive pattern of elliptical arcs surrounding the central region of the cluster. Why do the background galaxies appear stretched out elliptically in Figure 10.1? Consider a circular galaxy sitting behind a large mass density with an observer out of the page as in Figure 10.2a. Since the light rays are distorted, we do not expect to see a circular image. Rather, light rays coming from the "bottom" of this source — the ones that pass closer to the central mass region — are bent more than those that do not come as close to the mass. The light rays are bent such that objects at the bottom appear to be *farther away* from

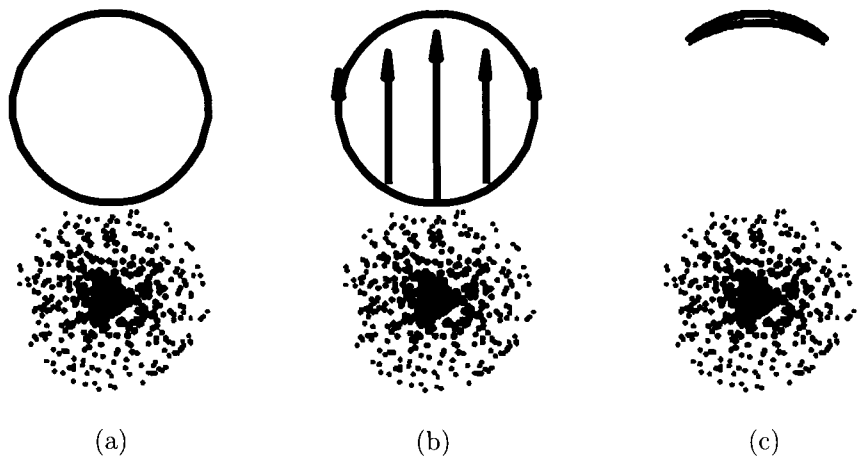

Figure 10.2. (a) Circular galaxy, the source, sits behind a foreground mass distribution represented by points at bottom. The observer is out of the page so that the foreground mass is between the observer and the source. (b) Light rays from source are deflected as they pass by mass distribution. Rays traveling closest to mass get deflected the most. (c) Resulting image is an arc.

the mass. (This is the only subtle part of the argument: rays are bent *toward* the mass distribution, so that as you extrapolate backward, the source appears farther away. See Figure 10.4.) Images will therefore be distorted as in Figure 10.2b. The net effect, therefore, is to turn a circular galaxy into the arc shown in panel c.

A very active field of research uses background galaxies to try to infer the mass distribution of clusters (e.g., Clowe *et al.*, 1998). Most times, the images are not as dramatic as those shown in Figure 10.1. The lack of drama is offset by the huge numbers of background galaxies. By adding up many small distortions, observers have succeeded in obtaining mass estimates for a number of clusters. This idea of statistically averaging small distortions is the hallmark of *weak lensing.* The mass estimates are important information for cosmologists: several cosmological constraints are based on cluster masses and abundances (e.g., Section 9.5, Carlberg *et al.*, 1997; Bahcall *et al.*, 2000).

We will be interested in weak lensing not by a single identifiable lens such as a cluster, but rather by the generic large-scale structure in the universe. Inferring the distribution of the dark matter — i.e., pointing to a spot on the sky and identifying it as an overdense region — is not necessarily the goal. Rather, we should be satisfied if we can measure some simple statistics, for example the correlation function or its Fourier transform, the power spectrum. Indeed, these are the quantities we, as cosmologists, are most interested in anyway. We don't care where the overdense and underdense regions are; we simply want to compare theory with observations. So our main goal here is to relate the observations (which have already begun) of distortions of galaxy images to the underlying mass power spectrum.

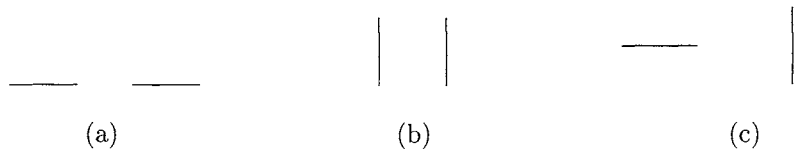

Figure 10.3. Different lensing patterns. Panels (a) and (b) could be produced by a mass distribution (a) above or below the distorted images and (b) in between or on either side of the images. But the alignment in panel (c) could not be produced by lensing.

One final note concerning the correlations of distortions expected from gravitational lensing. We might expect to find the images of two (circular) galaxies to be distorted so that they look like Figure 10.3a if, for example, there is a large overdensity above or beneath this galaxy pair. We might also expect images similar to those in Figure 10.3b if an overdensity exists between them or to either side. However, lensing cannot produce the alignment sketched in panel (c). This fact, which we will shortly prove, is often used as a check against systematic problems afflicting an observation.

10.2 GEODESICS AND SHEAR

We want to solve for the path of a light ray as it leaves a distant source and travels through the inhomogeneous universe. Figure 10.4 shows the geometry and notation, which will be similar to that set up in our discussion of the angular correlation function. The position of the photon at any time is given by $\vec{x}$, with the x_3 component equal to the radial distance χ and the transverse components equal to $\chi\vec{\theta}$. The intensity we observe from a source is

$$I_{\rm obs}(\vec{\theta}) = I_{\rm true}(\vec{\theta}_S); \tag{10.1}$$

a source whose image appears at $\vec{\theta}$ is actually at $\vec{\theta}_S$.

To solve for the path of a light ray, we need to use the machinery of general relativity. Recall that in Chapter 4, we used the time component of the geodesic equation to find dp/dt, the rate of change of the magnitude of the momentum. Here we are interested in deflections, so we will need the spatial component,

$$\frac{d^2x^i}{d\lambda^2} = -\Gamma^i_{\alpha\beta}\frac{dx^\alpha}{d\lambda}\frac{dx^\beta}{d\lambda}; \tag{10.2}$$

in particular, we will need the transverse part. Let's first consider the left side of this equation. We can express the derivatives with respect to affine parameter λ in terms of derivatives with respect to χ using the fact that

$$\frac{d\chi}{d\lambda} = \frac{d\chi}{dt}\frac{dt}{d\lambda}$$

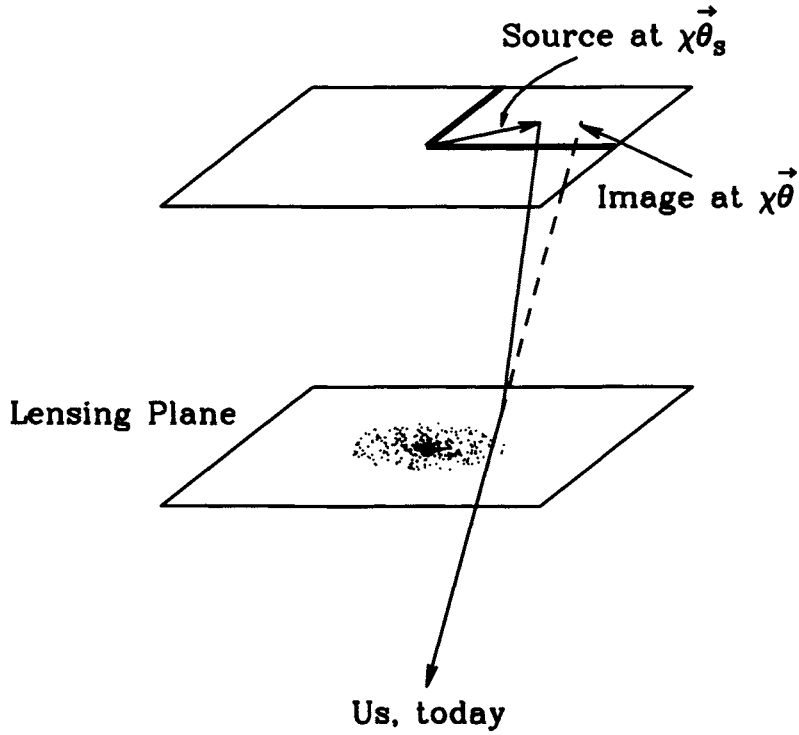

Figure 10.4. A light ray leaving a distance source is distorted as it passes by an intervening overdense region. At all times, the position of the light ray can be characterized by a 2D vector specifying its angular distance from the center of the lens. The ray starts with angular vector $\vec{\theta}_S$, but appears to us to be coming from $\vec{\theta}$.

$$= \frac{-1}{a} p(1 - \Psi). \tag{10.3}$$

The first part of this equality ($d\chi/dt = -1/a$) follows from Eq. (2.42), while the second part comes from Eq. (4.14). The transverse part of $\vec{x}^i$ is equal to $\chi\theta^i$, so the left-hand side of the geodesic equation is

$$\frac{d^2x^i}{d\lambda^2} = \frac{1}{a} p \frac{d}{d\chi}\left[\frac{p}{a}\frac{d}{d\chi}\left(\chi\theta^i\right)\right]. \tag{10.4}$$

Here I have dropped the (small) gravitational potential because it multiplies the (small) angle θ^i. We can reduce further by remembering that (at zero order) the momentum p times a remains constant, so removing pa outside the derivative leads to

$$\frac{d^2x^i}{d\lambda^2} = p^2 \frac{d}{d\chi}\left[\frac{1}{a^2}\frac{d}{d\chi}\left(\chi\theta^i\right)\right]. \tag{10.5}$$

Now let's consider the right side of the geodesic equation. Again, changing the derivatives with respect to λ to those with respect to χ leads to

$$\Gamma^i_{\alpha\beta}\frac{dx^\alpha}{d\lambda}\frac{dx^\beta}{d\lambda} = \left(\frac{p}{a}\right)^2 (1-\Psi)^2\Gamma^i_{\alpha\beta}\frac{dx^\alpha}{d\chi}\frac{dx^\beta}{d\chi}. \tag{10.6}$$

There are three types of terms in the sum over α and β: those with $\alpha = \beta = 0$, those with one index spatial and the other temporal, and finally those in which both α and β are spatial. We have already derived the relevant Christoffel symbols, given in Eq. (5.7). Let's work through the terms one by one:

- When $\alpha = \beta = 0$, we have

$$\Gamma^i_{00}\left(\frac{dt}{d\chi}\right)^2 = \Psi_{,i} = -\Phi_{,i} \tag{10.7}$$

  where the second equality holds since in the late universe there are no anisotropic stresses so $\Phi = -\Psi$.
- When one of the indices is spatial, Γ^i_{0j} is nonzero only when $i = j$. Therefore, the spatial index j must be transverse with $x^j = \chi\theta^j$. Since θ^j is small, we can drop the potential in the Christoffel symbol leading to

$$\Gamma^i_{0j}\frac{dt}{d\chi}\frac{dx^j}{d\chi} = -aH\frac{d}{d\chi}\left[\chi\theta^i\right] \tag{10.8}$$

  with of course an identical term coming from Γ^i_{j0}.
- When both indices are spatial, the Christoffel symbol is proportional to the (small) gravitational potential. When multiplied by the small transverse distance, these terms will be negligible, so we need consider only the term $\Gamma^i_{jk}(dx^j/d\chi)(dx^k/d\chi)$ in which $j = k = 3$ along the radial direction. In that case $x^3 = \chi$, the derivative is trivial, and we have

$$\Gamma^i_{jk}\frac{dx^j}{d\chi}\frac{dx^k}{d\chi} = -\Phi_{,i}. \tag{10.9}$$

Collecting these terms leads to the geodesic equation for transverse motion,

$$\frac{d}{d\chi}\left[\frac{1}{a^2}\frac{d}{d\chi}\left(\chi\theta^i\right)\right] = \frac{2}{a^2}\left[\Phi_{,i} + aH\frac{d}{d\chi}\left[\chi\theta^i\right]\right]. \tag{10.10}$$

The derivative on the left acting on a^{-2} exactly cancels the term proportional to aH on the right, so our final equation for the transverse displacement is

$$\frac{d^2}{d\chi^2}\left(\chi\theta^i\right) = 2\Phi_{,i}. \tag{10.11}$$

This geodesic equation tells us that in a uniform potential, the angular direction $(\chi\theta^i)'$ remains constant, whereas a changing potential perturbs it. The sign is correct: An overdensity centered at $x = y = 0$ has $\Phi > 0$ there, and therefore the derivative of Φ with respect to x ($\Phi_{,i}$ with $i = 1$) is negative for $x > 0$. As such, the force on a light ray passing the overdensity on the positive x-axis is negative, i.e., inward toward the overdensity, as we expect.

Equation (10.11) can be integrated to find the image angle as a function of the source angle. Integrating once gives

$$\frac{d}{d\chi}\left(\chi\theta^i\right) = 2\int_0^\chi d\chi' \Phi_{,i}\left(\vec{x}(\chi')\right) + \text{constant}; \tag{10.12}$$

we'll fix the constant momentarily. Integrating again leads to

$$\theta_S^i = \frac{2}{\chi}\int_0^\chi d\chi'' \int_0^{\chi''} d\chi' \Phi_{,i}\left(\vec{x}(\chi')\right) + \text{constant} \tag{10.13}$$

since $\theta^i(\chi) \equiv \theta_S^i$, the value of $\vec{\theta}$ at the source. We now see that the constant is equal to θ^i — the observed angle — since the angle retains its initial value if there is no perturbation. The integral in the χ', χ'' plane is restricted to the shaded region in Figure 10.5 so we can change orders of integration with the χ'' integral ranging

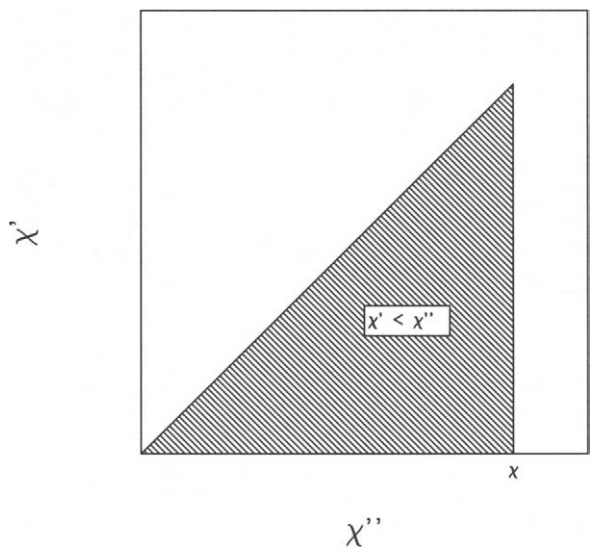

Figure 10.5. Range of integration in the double integral of Eq. (10.13). The shaded region can be expressed as $0 < \chi'' < \chi, 0 < \chi' < \chi''$ or as $\chi' < \chi'' < \chi, 0 < \chi' < \chi$. The latter is more convenient here, since the χ'' integral is then trivial.

from χ' to χ. The χ'' integral is then trivial (since $\Phi_{,i}$ depends only on χ') so

$$\theta_S^i = \theta^i + 2\int_0^\chi d\chi' \Phi_{,i}\left(\vec{x}(\chi')\right)\left(1 - \frac{\chi'}{\chi}\right). \tag{10.14}$$

To describe the shift in the angle experienced by a light ray, it is conventional to define the 2×2 symmetric transformation matrix,

$$A_{ij} \equiv \frac{\partial\theta_S^i}{\partial\theta^j}$$

$$\equiv \begin{pmatrix} 1-\kappa-\gamma_1 & -\gamma_2 \\ -\gamma_2 & 1-\kappa+\gamma_1 \end{pmatrix}. \tag{10.15}$$

The parameter κ is called the *convergence*; it describes how an image is magnified. Although this magnification has many important ramifications (e.g., microlensing and multiple images) it is not what is important for the distortions studied in weak lensing. Rather, these distortions are governed by the two components of the *shear*,

$$\gamma_1 = -\frac{A_{11}-A_{22}}{2}$$

$$\gamma_2 = -A_{12}. \tag{10.16}$$

Equation (10.15) says that the components of shear involve derivatives of Eq. (10.14) with respect to angle $\vec{\theta}$.[1] The only dependence on $\vec{\theta}$ is in the argument of the potential, where $\vec{x}(\chi') = \chi'\vec{\theta}$ (for the transverse components). Therefore, the derivative with respect to θ^j can be written as a derivative with respect to x^j (in our notation $_{,j}$) times χ'. Therefore,

$$A_{ij} - \delta_{ij} = \begin{pmatrix} -\kappa-\gamma_1 & -\gamma_2 \\ -\gamma_2 & -\kappa+\gamma_1 \end{pmatrix} = 2\int_0^\chi d\chi' \Phi_{,ij}\left(\vec{x}(\chi')\right)\chi'\left(1-\frac{\chi'}{\chi}\right). \tag{10.17}$$

So γ_1 and γ_2 are well-defined functions of the potential. The next section shows how they influence the shapes of galaxy images.

10.3 ELLIPTICITY AS AN ESTIMATOR OF SHEAR

We expect lensing to turn circular images into elliptical ones. To describe this effect, then, we need to come up with quantitative measures of ellipticity, and then see how these are related to the components of shear defined above. The simplest measure of ellipticity starts with the definition of the quadrupole moments of an image. Imagine centering an image at the $\theta_x - \theta_y$ origin such that it has no dipole moment ($\langle\theta_x\rangle = \langle\theta_y\rangle = 0$ where angular brackets are averages over the intensity). Then the quadrupole moments are defined as

$$q_{ij} \equiv \int d^2\theta I_{\rm obs}(\theta)\theta_i\theta_j. \tag{10.18}$$

A circular image has $q_{xx} = q_{yy}$ and $q_{xy} = 0$. Therefore, two good measures of ellipticity are

$$\epsilon_1 \equiv \frac{q_{xx}-q_{yy}}{q_{xx}+q_{yy}}$$

[1]The derivative is formally with respect to the observed angle $\vec{\theta}$, while the right-hand side of Eq. (10.14) depends on the potential at the true position of the light ray. In principle, then, the derivatives which go into the definition of A_{ij} are quite complicated. In practice, though, deflections are sufficiently small that we can ignore the distinction between the final angle $\vec{\theta}$ and the actual angle everywhere along the trajectory. Therefore, on the right-hand side of Eq. (10.14) we evaluate the potential along the undistorted path parameterized by $\vec{\theta}$.

$$\epsilon_2 \equiv \frac{2q_{xy}}{q_{xx} + q_{yy}}. \tag{10.19}$$

Figure 10.6 shows different orientations of elliptical images and the associated

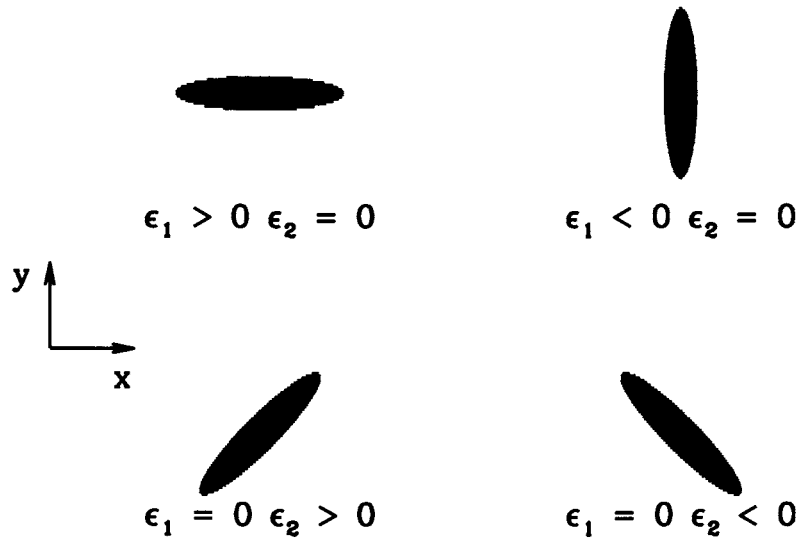

Figure 10.6. Definition of ellipticities ϵ_1 and ϵ_2. Circular images have both ellipticities equal to zero.

values of the ϵ_1 and ϵ_2. With these definitions, we can make more precise the statement at the end of Section 10.1 about correlations of ellipticities. Panel (a) in Figure 10.3 has two galaxies at $\vec{\theta}_1$ and $\vec{\theta}_2$, each with ϵ_1 positive; in panel (b) both galaxies have ϵ_1 negative. In both possible cases, then, the product $\epsilon_1(\vec{\theta}_1)\epsilon_1(\vec{\theta}_2)$ is positive if the x-axis is chosen along the direction connecting the two galaxies. The impossible case is depicted in panel (c) wherein the product is negative. Therefore, we do not expect lensing to produce $\epsilon_1(\vec{\theta}_1)\epsilon_1(\vec{\theta}_2) < 0$.

How are the ellipticities defined in Eq. (10.19) related to the shear defined in Eq. (10.16)? Let's assume that the source is spherical and compute the ellipticity of the image. Focusing on ϵ_1, we have

$$\epsilon_1 = \frac{\int d^2\theta I_{\rm true}(\vec{\theta}_S)\,[\theta_x\theta_x - \theta_y\theta_y]}{\int d^2\theta I_{\rm true}(\vec{\theta}_S)\,[\theta_x\theta_x + \theta_y\theta_y]} \tag{10.20}$$

where I have used the equality of Eq. (10.1). The integrals here are over the observed angles $\vec{\theta}$, while the integrands depend in part on the angle from which the photon started at the source, $\vec{\theta}_S$. For small angles, these are related via $\theta_i = (A^{-1})_{ij}\theta_{Sj}$. To do the integrals, then, change dummy variables in the integral to $\vec{\theta}_S$, and write all occurences of θ_i as $(A^{-1}\theta_S)_i$. This leads to

$$\epsilon_1 = \frac{\sum_{ij}\left[(A^{-1})_{xi}(A^{-1})_{xj} - (A^{-1})_{yi}(A^{-1})_{yj}\right]\int d^2\theta_S I_{\rm true}(\vec{\theta}_S)\theta_{Si}\theta_{Sj}}{\sum_{ij}\left[(A^{-1})_{xi}(A^{-1})_{xj} + (A^{-1})_{yi}(A^{-1})_{yj}\right]\int d^2\theta_S I_{\rm true}(\vec{\theta}_S)\theta_{Si}\theta_{Sj}}. \quad (10.21)$$

Now the integral over the (true) circular image vanishes unless $i = j$ and so is proportional to δ_{ij}. The proportionality constant is irrelevant since it appears in both the numerator and denominator, so

$$\begin{aligned}\epsilon_1 &= \frac{(A^{-1})_{xi}(A^{-1})_{xi} - (A^{-1})_{yi}(A^{-1})_{yi}}{(A^{-1})_{xi}(A^{-1})_{xi} + (A^{-1})_{yi}(A^{-1})_{yi}} \\ &= \frac{\left(A^{-1}_{xx}\right)^2 - \left(A^{-1}_{yy}\right)^2}{\left(A^{-1}_{xx}\right)^2 + \left(A^{-1}_{yy}\right)^2 + 2\left(A^{-1}_{xy}\right)^2}. \end{aligned} \quad (10.22)$$

It is easy to compute the inverse of the 2×2 matrix A:

$$A^{-1} = \frac{1}{(1-\kappa)^2 - \gamma_1^2 - \gamma_2^2}\begin{pmatrix} 1-\kappa+\gamma_1 & \gamma_2 \\ \gamma_2 & 1-\kappa-\gamma_1 \end{pmatrix}, \quad (10.23)$$

so we see that the ellipticity ϵ_1 can be expressed in terms of the shear as

$$\begin{aligned}\epsilon_1 &= \frac{(1-\kappa+\gamma_1)^2 - (1-\kappa-\gamma_1)^2}{(1-\kappa+\gamma_1)^2 + (1-\kappa-\gamma_1)^2 + 2\gamma_2^2} \\ &= \frac{4\gamma_1(1-\kappa)}{2(1-\kappa)^2 + 2\gamma_1^2 + 2\gamma_2^2}. \end{aligned} \quad (10.24)$$

If all the distortions are small, then

$$\epsilon_1 \simeq 2\gamma_1, \quad (10.25)$$

the desired result. A similar equality holds for ϵ_2. By measuring ellipticities of distant galaxies, therefore, we can get an estimate of the shear field, a field which depends manifestly on the underlying gravitational potential via Eq. (10.17).

10.4 WEAK LENSING POWER SPECTRUM

We can now compute the simplest statistics of the shear field, which can be estimated by measuring background galaxy ellipticities. Let's remove the identity from the transformation matrix A,

$$\psi_{ij} \equiv A_{ij} - \delta_{ij}. \quad (10.26)$$

In the absence of inhomogeneities, the apparent angle θ is equal to the source angle θ_S, so $A = I$. Therefore, by removing the identity matrix from A, we have extracted the part describing the distortion of the light ray path due to inhomogeneities. As such, we will refer to ψ as the *distortion* tensor. The last term in (10.17) is ψ_{ij} for a background galaxy (or galaxies) at distance $\chi(z)$ from us. In general, a survey

contains a distribution of redshifts. Let's call this distribution $W(\chi)$, just as we did when studying angular correlations in Chapter 9. Again, let's normalize W so that $\int d\chi W(\chi) = 1$. Then, the distortion tensor is

$$\psi_{ij} = 2\int_0^{\chi_\infty} d\chi W(\chi) \int_0^{\chi} d\chi' \Phi_{,ij}\left(\vec{x}(\chi')\right) \chi' \left(1 - \frac{\chi'}{\chi}\right). \tag{10.27}$$

We can simplify here by changing orders of integration (almost exactly as depicted in Figure 10.5). Then

$$\psi_{ij}(\vec{\theta}) = \int_0^{\chi_\infty} d\chi \Phi_{,ij}\left(\vec{x}(\chi)\right) g(\chi) \tag{10.28}$$

where I have dropped the prime and defined

$$g(\chi) \equiv 2\chi \int_\chi^{\chi_\infty} d\chi' \left(1 - \frac{\chi}{\chi'}\right) W(\chi'). \tag{10.29}$$

On average, each of the components of the distortion tensor is zero: $\langle \psi_{ij} \rangle = 0$. To make our money, therefore, we need to do just what we did for the CMB and galaxy distributions, compute the two-point function, either the angular correlation functions of the different components of ψ_{ij} or their Fourier transforms, the power spectra. To compute these two-point functions, we will be able to essentially copy the results from Section 9.1 as long as we are careful to account for the indices on ψ_{ij}.

To compute the power spectrum of the distortion tensor, $P^{\psi}_{ijkl}(\vec{l})$, let's recall the steps we took when we analyzed the angular correlation function of galaxies (see Table 10.1).

- The distortion tensor in Eq. (10.28) is a function of the 2D vector $\vec{\theta}$ since the argument of the potential is $\vec{x} \simeq \chi(\theta_1, \theta_2, 1)$. As in the case of the galaxy density field, we can Fourier transform ψ_{ij} so that it depends on the 2D vector conjugate to $\vec{\theta}$, $\vec{l}$.
- In the case of the angular galaxy overdensity, we expressed the 2D overdensity as an integral over the 3D overdensity with some weighting function (Eq. (9.3)). Here the situation is identical: g in Eq. (10.29) plays the role of the selection function W there while the 3D field here is not the overdensity δ, but rather $\Phi_{,ij}$.
- Next we found that — in the small-angle limit — the 2D power spectrum is given by an integral over the 3D power spectrum, Eq. (9.10). Here, too, the 2D power spectrum of ψ_{ij} can be expressed as an integral over the 3D power spectrum of the gravitational potential Φ. The only slightly tricky part is computing the 3D power spectrum of $\Phi_{,ij}$. The Fourier transform of $\Phi_{,ij}$ is $-k_i k_j \tilde{\Phi}$ with a variance

$$k_i k_j k'_l k'_m \langle \tilde{\Phi}(\vec{k}) \tilde{\Phi}^*(\vec{k}') \rangle = (2\pi)^3 k_i k_j k_l k_m \delta^3(\vec{k} - \vec{k}') P_\Phi(k). \tag{10.30}$$

So the 3D power spectrum we need — the one associated with the Fourier transform of $\Phi_{,ij}$ – is $k_i k_j k_l k_m P_\Phi(k)$.

Table 10.1. Similarity between Agular Correlations of Galaxies and Weak Lensing.

	Angular galaxy distribution	Weak lensing
2D observation	$\delta_2(\vec{\theta})$	Distortion tensor $\psi_{ij}(\vec{\theta})$
Weighting function	$W(\chi)$	$g(\chi)$
3D field	δ	$\Phi_{,ij}$
3D power spectrum	$\langle\tilde{\delta}\tilde{\delta}^*\rangle \sim P(k)$	$\langle\tilde{\Phi}_{,ij}\tilde{\Phi}^*_{,lm}\rangle \sim k_i k_j k_l k_m P_\Phi(k)$
2D power spectrum	$P_2(l)$	$P^\psi_{ijlm}(\vec{l})$

I will keep things in terms of P_Φ, but if you are more comfortable with the density power spectrum, you can see from Eq. (7.7) that you need only multiply P_Φ by $9\Omega_m^2 H_0^4(1+z)^2/(4k^4)$. Applying Eq. (9.10) then leads to

$$\langle\tilde{\psi}_{ij}(\vec{l})\tilde{\psi}_{lm}(\vec{l}')\rangle = (2\pi)^2\delta^2(\vec{l}-\vec{l}')P^\psi_{ijlm}(\vec{l}) \tag{10.31}$$

with the 2D power spectrum

$$P^\psi_{ijlm}(\vec{l}) = \int_0^{\chi_\infty} d\chi \frac{g^2(\chi)}{\chi^2}\frac{l_i l_j l_l l_m}{\chi^4} P_\Phi(l/\chi). \tag{10.32}$$

Equation (10.32) is an expression for the power spectrum of the different components of the distortion tensor. We can turn these into power spectra for the convergence κ and two different components of shear by using Eq. (10.16). Let's work this out for one of the shear components explicitly; the other two are relegated to a problem. Since $\gamma_1 = (\psi_{22} - \psi_{11})/2$, the power spectrum of γ_1 is 1/4 times $P^\psi_{2222} + P^\psi_{1111} - 2P^\psi_{2211}$. If we decompose the 2D vector $\vec{l}$ into a radial part l and an angle ϕ_l, then $l_1 = l\cos\phi_l$ and $l_2 = l\sin\phi_l$, so

$$P_{\gamma_1}(l,\phi_l) = \left(\sin^4\phi_l + \cos^4\phi_l - 2\sin^2\phi_l\cos^2\phi_l\right)\left[\frac{l^4}{4}\int_0^{\chi_\infty} d\chi\frac{g^2(\chi)}{\chi^6}P_\Phi(l/\chi)\right]. \tag{10.33}$$

Since $\sin^4\phi_l + \cos^4\phi_l + 2\cos^2\phi_l\sin^2\phi_l = 1$, the term in parentheses here is equal to $1 - 4\sin^2\phi_l\cos^2\phi_l = 1 - \sin^2(2\phi_l)$ or $\cos^2(2\phi_l)$. You will show in Exercise 6 that the expression in square brackets is equal to the power spectrum of the convergence,

$$P_\kappa = \frac{l^4}{4}\int_0^{\chi_\infty} d\chi\frac{g^2(\chi)}{\chi^6}P_\Phi(l/\chi). \tag{10.34}$$

Therefore, the power spectrum of γ_1 is

$$P_{\gamma_1}(l,\phi_l) = \cos^2(2\phi_l)\ P_\kappa(l). \tag{10.35}$$

You will show in Exercise 6 that the power spectrum of γ_2 is also proportional to P_κ,

$$P_{\gamma_2}(l,\phi_l) = \sin^2(2\phi_l)\ P_\kappa(l). \tag{10.36}$$

Thus, the power spectra of the two components of shear depend not only on the magnitude of $\vec{l}$ but also on its direction. Figure 10.7 shows the convergence power

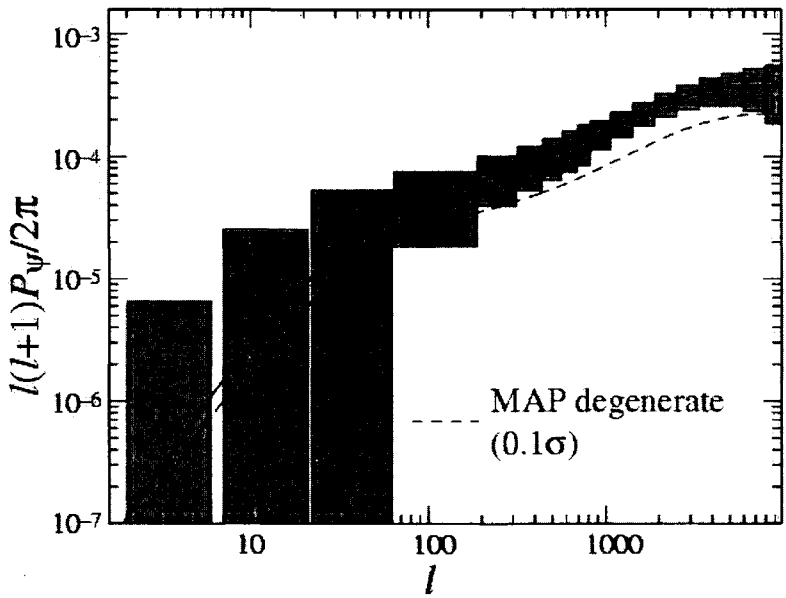

Figure 10.7. The power spectrum of the convergence for two CDM models (Hu and Tegmark, 1999). The models are indistinguishable using CMB data alone, so future weak lensing data (depicted by the error boxes) add invaluable information. The projected error boxes assume a 3° survey down to 25th magnitude.

spectrum for two models. Note that, unlike the CMB or even the matter power spectrum, it is essentially featureless.

The power spectra of both shear components are proportional to P_κ, with a prefactor depending on the angle between $\vec{l}$ and a fixed x-axis. You might expect then that a linear combination of the two components depends only on $P_\kappa(l)$ with no dependence on the angle ϕ_l. This is correct. Even more interesting, though, is the possibility that a different linear combination would have a vanishing power spectrum. This also turns out to be correct, and extremely useful. Such a mode has no expected cosmological signal, so any nonzero value is a measure of some systematic effect. By focusing on this "zero" mode, one can identify and eliminate contaminating effects in an experiment. I want to spend some time on this decomposition into two modes — one with signal and one without — not only because of its importance in this case of weak lensing, but also because an exact analogy exists in the case of polarization of the CMB, which we will take up in the next sections. To get ahead of myself, in the case of polarization, the "zero" mode is zero only for scalar perturbations, whereas tensor perturbations do contribute to it. Therefore, we will see in Section 10.9 that this decomposition is a powerful tool with which to detect primordial gravity waves.

Consider then the following two linear combinations of the shear:

$$E(\vec{l}) \equiv \cos(2\phi_l)\gamma_1(\vec{l}) + \sin(2\phi_l)\gamma_2(\vec{l})$$

$$B(\vec{l}) \equiv -\sin(2\phi_l)\gamma_1(\vec{l}) + \cos(2\phi_l)\gamma_2(\vec{l}). \tag{10.37}$$

The power spectrum of each of these modes is easily obtainable in terms of the spectra of γ_1 and γ_2. First the E-mode:

$$P_E = \cos^2(2\phi_l)P_{\gamma_1} + \sin^2(2\phi_l)P_{\gamma_2} + 2\sin(2\phi_l)\cos(2\phi_l)P_{\gamma_1\gamma_2}. \tag{10.38}$$

This expression involves the power spectrum corresponding to $\langle\gamma_1\gamma_2\rangle$, which is equal to $\cos(2\phi_l)\sin(2\phi_l)$ times the ubiquitous convergence power spectrum. Therefore, P_E is proportional to P_κ with proportionality constant $\cos^4(2\phi_l) + \sin^4(2\phi_l) + 2\cos^2(2\phi_l)\sin^2(2\phi_l) = (\cos^2(2\phi_l) + \sin^2(2\phi_l))^2 = 1$, or

$$P_E = P_\kappa, \tag{10.39}$$

independent of the angle ϕ_l. The calculation for the B-mode is similar:

$$\begin{aligned} P_B &= \sin^2(2\phi_l)P_{\gamma_1} + \cos^2(2\phi_l)P_{\gamma_2} - 2\sin(2\phi_l)\cos(2\phi_l)P_{\gamma_1\gamma_2} \\ &= 0. \end{aligned} \tag{10.40}$$

You can also check that the cross power spectrum $\langle EB\rangle$ vanishes.

The field of weak lensing due to large-scale structure is its infancy. The year 2000 saw the first detections by four independent groups (Van Waerbecke *et al.*, 2000; Bacon, Refregier, and Ellis, 2000; Wittman *et al.*, 2000; Kaiser, Wilson, and Luppino, 2000). They presented the shear correlation function, one example of which is shown in Figure 10.10. We can easily translate the power spectra derived above into angular correlation functions that can be compared with data.

Let's focus on the angular correlation function of γ_1, the Fourier transform of P_{γ_1},

$$w_{\gamma_1}(\vec{\theta}) = \int \frac{d^2l}{(2\pi)^2} e^{i\vec{l}\cdot\vec{\theta}} \cos^2(2\phi_l) \left[\frac{l^4}{4}\int_0^{\chi_\infty} d\chi \frac{g^2(\chi)}{\chi^6} P_\Phi(l/\chi)\right]. \tag{10.41}$$

The variable ϕ_l we are integrating over is the angle between the 2D vector $\vec{l}$ and an arbitrary external x-axis. If we do the angular integral over ϕ_l, then—as you can see from Figure 10.8—the argument of the exponential is quite complicated: $il\theta\cos(\phi_l - \phi)$. Instead, let's integrate over the angle between $\vec{l}$ and $\vec{\theta}$, call it ϕ'. Then,

$$w_{\gamma_1}(\vec{\theta}) = \int_0^\infty \frac{dl}{(2\pi)^2}\,\frac{l^5}{4}\int_0^{\chi_\infty} d\chi \frac{g^2(\chi)}{\chi^6} P_\Phi(l/\chi) \int_0^{2\pi} d\phi' e^{il\theta\cos\phi'} [\cos(2(\phi' + \phi))]^2. \tag{10.42}$$

The cosine squared in the integrand is equal to

$$\left[\cos(2\phi')\cos(2\phi) - \sin(2\phi')\sin(2\phi)\right]^2$$

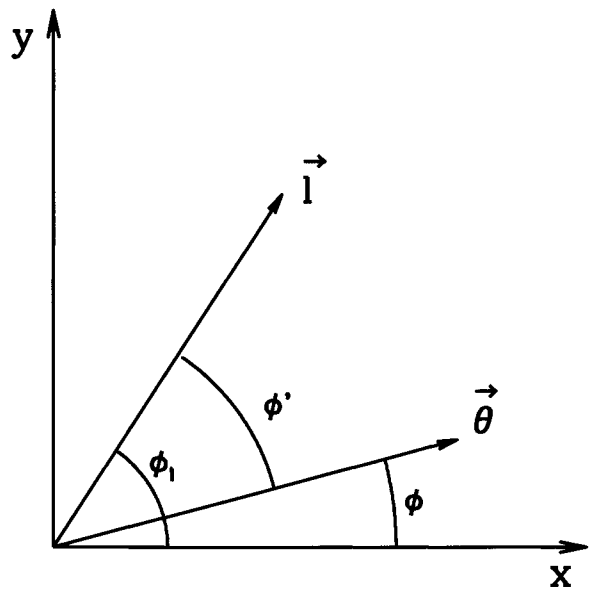

Figure 10.8. Angles made by $\vec{\theta}$ and $\vec{l}$ with respect to an external fixed x-y coordinate system. The angle between $\vec{\theta}$ and $\vec{l}$ is ϕ'.

$$= \cos^2(2\phi')\cos^2(2\phi) - \sin(4\phi')\sin(4\phi)/2 + \sin^2(2\phi')\sin^2(2\phi). \quad (10.43)$$

Thus there are three terms to be integrated over. To do the integral over $\cos^2(2\phi')$, first rewrite it as $(1+\cos(4\phi'))/2$; then recall that the integral of $\cos(n\phi')e^{iz\cos\phi'}$ is equal to $2\pi i^n J_n(z)$ (Eq. (C.21)). Therefore, the integral of $\cos^2(2\phi')$ gives a factor of π times $J_0(l\theta) + J_4(l\theta)$. Using exactly the same arguments, you can see that the integral of $\sin^2(2\phi')$ gives π times $J_0(l\theta) - J_4(l\theta)$. Less obvious is the fact that the integral of $\sin(4\phi')$ vanishes (change integration variable to $\phi'' = \phi' - \pi$ and argue that the integrand is antisymmetric). Therefore,

$$w_{\gamma_1}(\vec{\theta}) = \frac{1}{16\pi}\int_0^\infty dl\; l^5 \int_0^{\chi_\infty} d\chi \frac{g^2(\chi)}{\chi^6} P_\Phi(l/\chi)$$
$$\times\Big\{\cos^2(2\phi)\,[J_0(l\theta) + J_4(l\theta)] + \sin^2(2\phi)\,[J_0(l\theta) - J_4(l\theta)]\Big\}. \quad (10.44)$$

There are many angles floating around, so let me reiterate that $\vec{\theta} = (\theta\cos\phi, \theta\sin\phi)$; that is, ϕ is the angle that $\vec{\theta}$ makes with the x-axis. By changing the l integral into one over 3D wavenumber $k = l/\chi$, we can rewrite this angular correlation function in terms of kernels,

$$w_{\gamma_1}(\vec{\theta}) = \int_0^\infty dk\; k^5 P_\Phi(k)\left[F_+(k\theta)\cos^2(2\phi) + F_-(k\theta)\sin^2(2\phi)\right]. \quad (10.45)$$

Note that here I have assumed that the potential remains constant with time, an assumption which breaks down at late times because of nonlinearities or non-matter

domination. The kernels are integrals over radial distance χ modulated by the Bessel functions,

$$F_{\pm}(k\theta) \equiv \frac{1}{16\pi} \int_0^{\chi_\infty} d\chi g^2(\chi) \left[J_0(k\chi\theta) \pm J_4(k\chi\theta)\right]. \tag{10.46}$$

Figure 10.9 shows these two kernels for background galaxies at redshift $z = 0.9$.

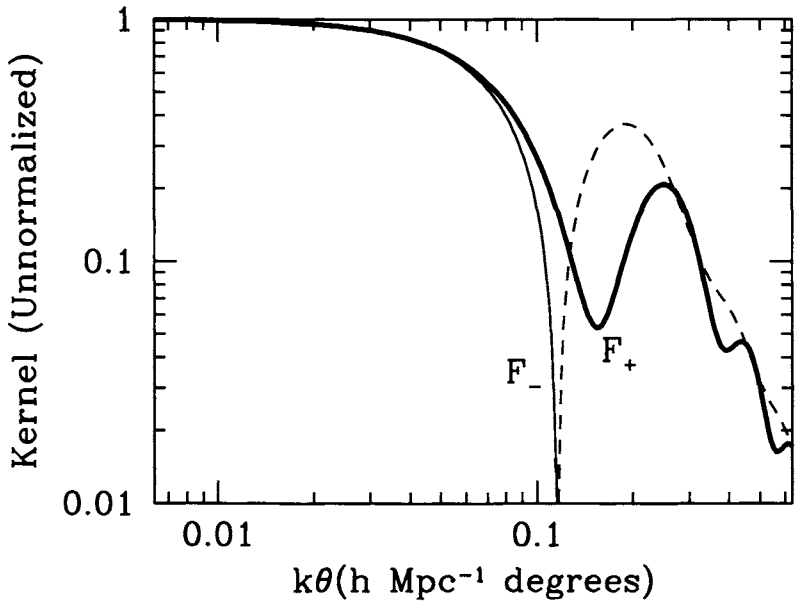

Figure 10.9. The kernels for the shear correlation function assuming all background galaxies are at $z = 0.9$. Dashed region corresponds to negative kernel. If the x-axis is chosen along the line connecting pairs of galaxies, then the + kernel is for $\langle\gamma_1\gamma_1\rangle$ and the − for $\langle\gamma_2\gamma_2\rangle$. Note that the former is always positive.

If we choose the x-axis to be along the line connecting pairs of galaxies, then we are evaluating the correlation function at $\vec{\theta} = (\theta, 0)$, that is, with $\phi = 0$. In that case, Figure 10.9 shows that w_{γ_1} is always positive, a result we anticipated pictorially in Section 10.1. The correlation function for γ_2, on the other hand, is identical to that in Eq. (10.45) except that $F_{\pm}$ are interchanged. Therefore, w_{γ_2} can, and indeed does, go negative, usually on large angular scales. The final point to take away from the kernels in Figures 10.9 is the rough sense that the shear on a scale of a tenth of degree probes the power spectrum at $k \sim 1\,h$ Mpc^{-1} since this is where the kernel breaks.

Consider then Figure 10.10, which shows results from a survey of three "blank" (i.e., no known clusters of galaxies present) fields over a period of several years. There is a clear detection of ellipticity, presumably due to cosmic shear. The root mean square amplitude of the shear is the square root of the typical numbers on the y-axis, around 0.01. Thus, shear due to large-scale structure has been detected

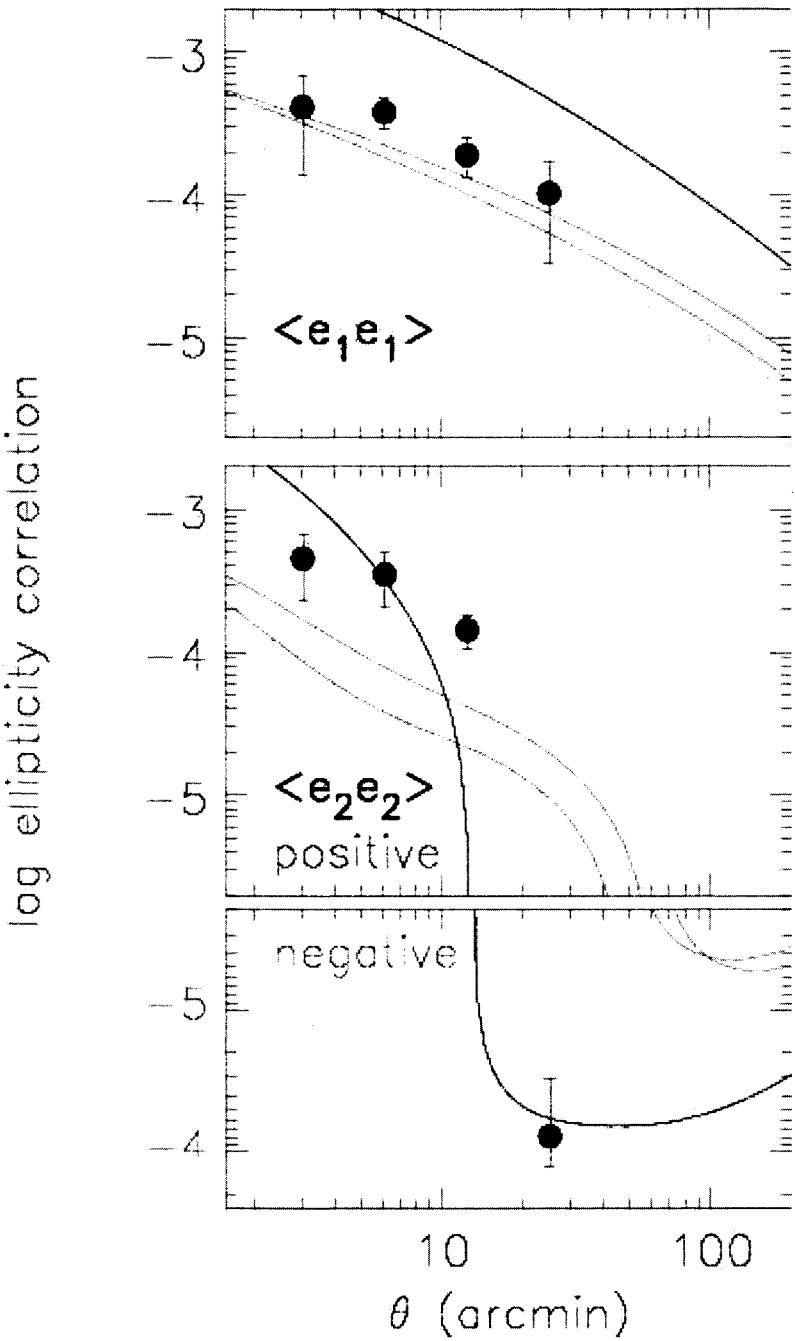

Figure 10.10. Measurement of the shear correlation functions using $145,000$ background galaxies (Wittman *et al.*, 2000). Also shown are a variety of CDM models; topmost in top panel is standard CDM, ruled out here at many sigma. Note that $w_{\gamma_1} = \langle e_1 e_1 \rangle$ remains positive on all angular scales. See color Plate 10.10.

with an amplitudeof order 10^{-2} on angular scales ranging from $1'$ out to about $1°$. Observations planned in the coming years will go far beyond these preliminary results; from these observations we will learn much about the mass distribution of the universe.

10.5 POLARIZATION: THE QUADRUPOLE AND THE Q/U DECOMPOSITION

The radiation in the CMB is expected to be polarized because of Compton scattering at the time of decoupling. A polarization pattern shares a number of mathematical features with the shear induced by gravitational lensing that we have just studied. In addition to these mathematical similarities, they also share similar experimental histories. Whereas anisotropies in the temperature of the CMB and inhomogeneities in the density field were discovered back in the 20th century, weak lensing by large scale structure and polarization of the CMB have just been detected. They are true 21st century phenomena. Therefore, they are both fields rich for study: We are just beginning our observations of them, and they both promise to deliver much cosmological information.

Light traveling in the x-direction corresponds to electric and magnetic fields oscillating in the y-z plane, i.e., transverse to the direction of propagation. If the intensity along the two transverse directions is equal, then the light is unpolarized. Until now, when we have considered the CMB, we have been implicitly studying this case. Now we must account for the possibility that the intensities in the two transverse directions are unequal: that the radiation is polarized.

At first glance, Compton scattering is a perfect mechanism for producing polarized radiation. It allows all transverse radiation to pass through unimpeded, while completely stopping any radiation parallel to the outgoing direction. To see this, consider Figure 10.11 which shows a ray incident from the $+\hat{x}$ direction. This (unpolarized) ray has equal intensity in the $\hat{y}$ and $\hat{z}$ directions. It scatters off an electron at the origin and gets deflected into the $+\hat{z}$ direction.[2] Since the outgoing direction is along the z-axis, none of the (incoming) intensity along the z-axis gets transmitted. By contrast, all of the intensity along the y-axis (which is perpendicular to both the incoming and outgoing directions) is transmitted. The net result is outgoing polarization in the $\hat{y}$ direction.

Obviously, we cannot content ourselves with studying one incoming ray; we must generalize to radiation incident on an electron from all directions. When we do so, we begin to realize that producing polarization will not be quite as easy as it appears from Figure 10.11. Consider first Figure 10.12, which shows a caricature of a much more relevant case: isotropic radiation incident on the electron from all directions. I say "caricature" because I have shown incoming rays from only two directions, the $+\hat{x}$- and $+\hat{y}$-directions. The intensity of the outgoing ray along the

[2]Of course radiation gets scattered into all directions with varying probability. Here we consider just one outgoing direction for simplicity. In the next section we account for this probability.

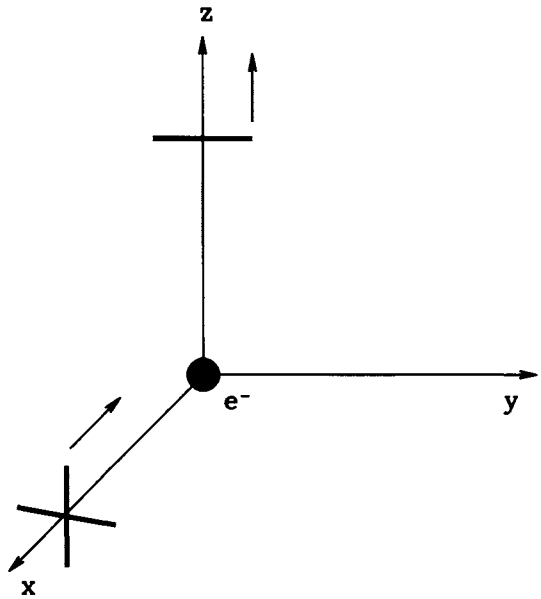

Figure 10.11. Unpolarized radiation moving toward the origin along the x-axis is scattered by an electron into the $+\hat{z}$ direction. Only the $\hat{y}$ component of the radiation remains after scattering. Since there was no incoming $\hat{x}$ polarization, the outgoing radiation is polarized in the $\hat{y}$ direction. (This and the next three figures are adapted from Hu and White, 1997b).

x-axis comes from the radiation incident from the $\hat{y}$ direction, while the outgoing y-intensity comes from the radiation incident from the $\hat{x}$-axis. Since the radiation from both directions has equal intensity (isotropic radiation), though, the outgoing wave is has equal intensity along the $\hat{x}$- and $\hat{y}$-axes: it is unpolarized.

Can anisotropic radiation produce polarization? The simplest example of anisotropy is a dipole pattern, a caricature of which is shown in Figure 10.13. Now the outgoing intensity along the x-axis comes from the $\pm\hat{y}$-incident radiation, which has the average temperature. The outgoing intensity along the y-axis is also neither hot nor cold because it comes from a cold spot (the $-\hat{x}$-direction) and a hot spot (the $+\hat{x}$-direction). The dipole pattern leads therefore only to cancellations and unpolarized outgoing radiation.

To produce polarized radiation, the incoming radiation must have a nonzero quadrupole. Figure 10.14 illustrates the polarization produced by an incoming quadrupole. The hotter (colder) radiation incident from the $\hat{x}$- ($\hat{y}$-) direction produces higher (lower) intensity along the y- (x-) axis for the outgoing wave. Therefore, the intensity of the outgoing wave is greater along the y-axis than along the x-axis: the outgoing radiation is polarized.

The fact that Compton scattering produces polarization only when the incident field has a quadrupole moment has important ramifications for cosmology. We need Compton scattering to produce the polarization, so we need to focus on the epoch

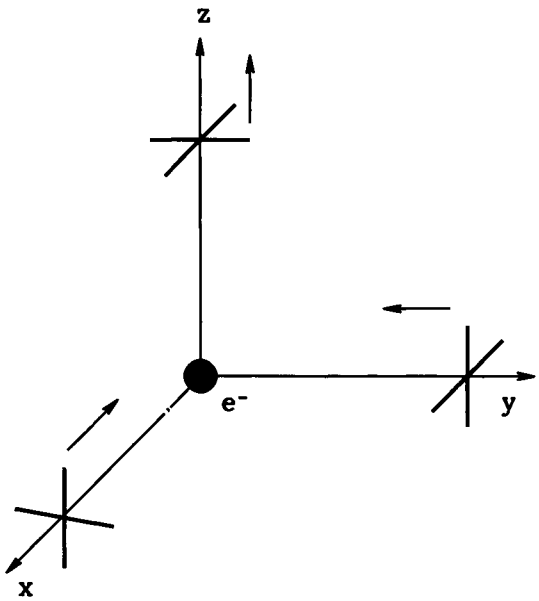

Figure 10.12. Incoming isotropic radiation produces no polarization. Here, since the incoming amplitudes from the $\hat{x}$- and $\hat{y}$-directions are equal, the outgoing intensities along both of these directions are equal, leading to unpolarized radiation.

before electrons and photons have completely decoupled from each other. However, in this epoch electrons and photons are tightly coupled, which we have seen leads to a very small quadrupole. Therefore, we expect polarization from the standard decoupling epoch to be smaller than the anisotropies. Late reionization enhances the polarization at large scales, but does not modify the qualitative conclusion that the polarization signal is expected to be small.

Figure 10.14 depicts polarization in the x-y plane, preferentially in the $\hat{y}$-direction. Alternatively, had the incoming rays been rotated by 45° in the x-y plane, the outgoing polarization would have been along the axis 45° from the x- and y-axes. Polarization therefore can be depicted as a headless vector, with a length corresponding to its magnitude and the orientation of the line describing the axis along which the intensity is greatest. In the 2D plane perpendicular to the direction of propagation, we therefore decompose the intensity into

$$I_{ij} = \begin{pmatrix} T+Q & U \\ U & T-Q \end{pmatrix}. \tag{10.47}$$

The diagonal elements T are the temperature we studied in Chapter 8 (with a uniform part and a perturbation Θ); the two new variables Q and U describe polarization. The pattern in Figure 10.14 has $Q < 0$ and $U = 0$. Note that these definitions of Q and U are identical to the definitions of shear and ellipticity in Section 10.2. Especially relevant is Figure 10.6 where we simply replace ϵ_1 with Q

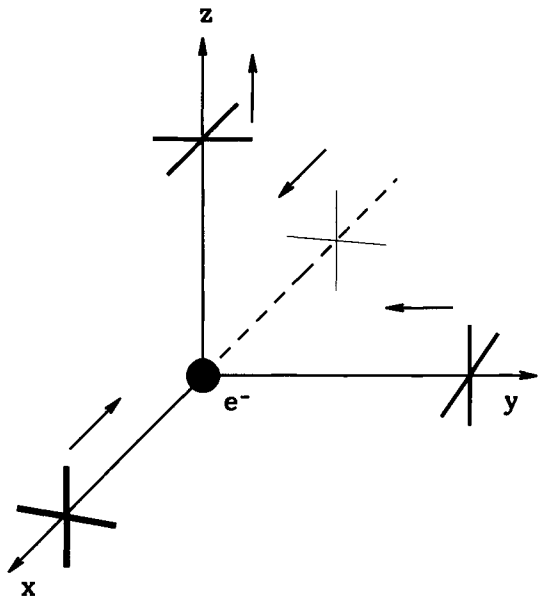

Figure 10.13. Incoming dipole radiation also produces no polarization. (See also color Plate 10.13.) Heavy (thin) lines denote hot (cold) spots. Here the incoming radiation is hotter than average (average is medium thickness) from the $+\hat{x}$-direction, and colder than average from the $-\hat{x}$-direction. The two rays from the $\pm\hat{x}$-directions therefore produce the average intensity for the outgoing ray along the $\hat{y}$-direction. The outgoing intensity along the $\hat{x}$-direction is produced by the ray incident from the $\pm\hat{y}$-directions. Since these have the average intensity, the outgoing intensity is also the average along the $\hat{x}$-direction. The net result is outgoing unpolarized light.

and ϵ_2 with U. A final note: students of electricity and magnetism will no doubt recognize T, Q, and U as three of the four Stokes parameters used to describe polarization. The fourth, V, is nonzero only if polarization is circularly polarized, a phenomenon we do not expect in the early universe, so I have implicitly set $V = 0$ here.

10.6 POLARIZATION FROM A SINGLE PLANE WAVE

The pictures of the previous subsection are important to gain a qualitative understanding of how Compton scattering produces polarization, but they are inefficient tools with which to study the phenomenon quantitatively. The proper tool is the Boltzmann equation. We could proceed now by simply writing down the Boltzmann equation for the Q and U polarization states. In doing so, however, we would lose some of the intuition just gained, so I will take an intermediate tack. We will generalize the discussion of the previous section by summing over all incident rays, not just a handful. This will enable us to make the connection with the distribution Θ

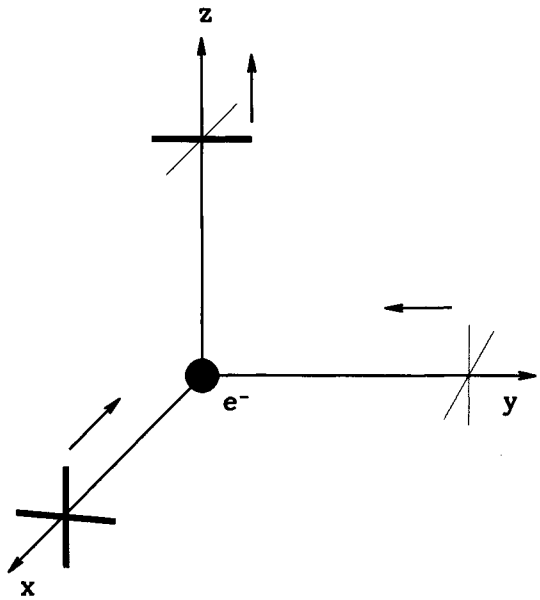

Figure 10.14. Incoming quadrupole radiation produces outgoing polarized light. See also color Plate 10.14.) The outgoing radiation has greater intensity along the y-axis than in the $\hat{x}$-direction. This is a direct result of the hotter radiation incident from the $\hat{x}$-direction.

we have used until now to characterize the photons.

We first need to define the polarization axes in the most general case when the incoming photon arrives from direction $\hat{n}'$. When that direction was $\hat{x}$, as in the previous section, it was clear that polarization was defined as the difference in the intensity along the two perpendicular directions, $\hat{y}$ and $\hat{z}$. In the general case, depicted in Figure 10.15, the direction of the incoming photon is depicted by $\hat{n}'$, and we must integrate over all incoming directions. The two axes perpendicular to this direction are most conveniently taken to be $\hat{\theta}'$ and $\hat{\phi}'$, the standard unit vectors perpendicular to the position vector. These are called $\hat{\epsilon}'_1$ and $\hat{\epsilon}'_2$. We still are interested in the polarization of outgoing photons in the $\hat{z}$-direction, so we can choose the two outgoing polarization axes as $\hat{\epsilon}_1 = \hat{x}$ and $\hat{\epsilon}_2 = \hat{y}$. In short, the incoming polarization vectors are $\hat{\epsilon}'_i$, the outgoing are $\hat{\epsilon}_i$.

The idea that Compton scattering allows the fields transverse to the outgoing direction to pass through unimpeded, while stopping those parallel to the outgoing direction, can be encapsulated by saying that the cross-section for outgoing photons polarized in the $\hat{\epsilon}_i$ direction is proportional to

$$\sum_{j=1}^{2} \left|\hat{\epsilon}_i(\hat{n}) \cdot \hat{\epsilon}'_j(\hat{n}')\right|^2 . \tag{10.48}$$

The Q polarization is the difference between this cross-section for $i = 1$ and $i = 2$, i.e., the difference between the field strength in $\hat{x}$- and $\hat{y}$-directions:

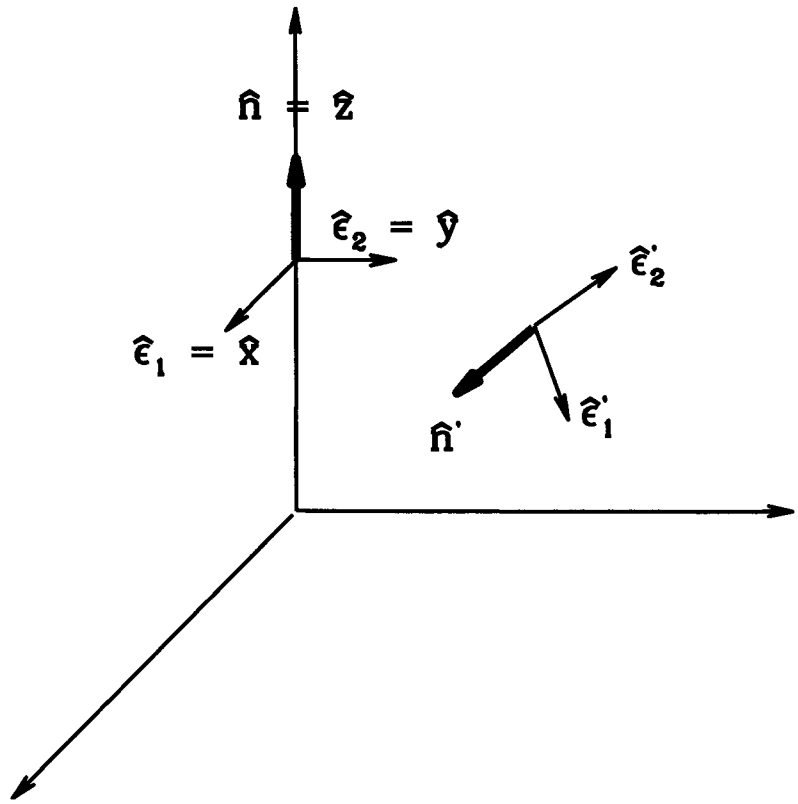

Figure 10.15. Incoming photon from direction $\hat{n}'$ Compton scatters off an electron at the origin producing outgoing photon in direction $\hat{n} = \hat{z}$. The plane perpendicular to the incoming direction is spanned by the two polarization vectors, $\hat{\epsilon}'_1 = \hat{\theta}'$ and $\hat{\epsilon}'_2 = \hat{\phi}'$. The outgoing photon is in the $\hat{z}$ direction, so the polarization vectors are $\hat{\epsilon}_1 = \hat{x}$ and $\hat{\epsilon}_2 = \hat{y}$.

$$\sum_{j=1}^{2} \left|\hat{\epsilon}_1(\hat{n}) \cdot \hat{\epsilon}'_j(\hat{n}')\right|^2 - \sum_{j=1}^{2} \left|\hat{\epsilon}_2(\hat{n}) \cdot \hat{\epsilon}'_j(\hat{n}')\right|^2 = \sum_{j=1}^{2} \left(\left|\hat{x} \cdot \hat{\epsilon}'_j(\hat{n}')\right|^2 - \left|\hat{y} \cdot \hat{\epsilon}'_j(\hat{n}')\right|^2 \right). \tag{10.49}$$

Integrating over all incoming $\hat{n}'$ directions leads to

$$Q(\hat{z}) = A \int d\Omega_{n'} f(\hat{n}') \sum_{j=1}^{2} \left(\left|\hat{x} \cdot \hat{\epsilon}'_j(\hat{n}')\right|^2 - \left|\hat{y} \cdot \hat{\epsilon}'_j(\hat{n}')\right|^2 \right). \tag{10.50}$$

Here A is a normalization constant which will not concern us for now, and $f(\hat{n}')$ is the intensity of the radiation incoming from the $\hat{n}'$-direction, and we integrate over all such directions. Note that f depends only on $\hat{n}'$, but not on ϵ'_j: this corresponds to the assumption that the incident radiation is unpolarized.

To take the dot products in Eq. (10.50), we will find it useful to express $\hat{\epsilon}'_1$ and $\hat{\epsilon}'_2$ in terms of their Cartesian coordinates. Since they are equal to $\hat{\theta}'$ and $\hat{\phi}'$,

respectively, we have

$$\hat{\epsilon}'_1(\theta', \phi') = (\cos\theta' \cos\phi', \cos\theta' \sin\phi', -\sin\theta')$$
$$\hat{\epsilon}'_2(\theta', \phi') = (-\sin\phi', \cos\phi', 0)\,. \tag{10.51}$$

Now, the dot products become trivial, and we find

$$Q(\hat{z}) = A \int d\Omega_{n'} f(\hat{n}') \Big[\cos^2\theta' \cos^2\phi' + \sin^2\phi' - \cos^2\theta' \sin^2\phi' - \cos^2\phi' \Big]$$
$$= -A \int d\Omega_{n'} f(\hat{n}') \sin^2\theta' \cos 2\phi'. \tag{10.52}$$

You might recognize the combination of angles here as being propotional to the sum of the spherical harmonics $Y_{2,2} + Y_{2,-2}$ (Eq. (C.10)). Since the spherical harmonics are orthogonal, the integral will pick out the $l = 2, m = \pm 2$ components of the distribution f. That is, nonzero Q will be produced only if the incident radiation has a quadrupole moment. This verifies the argument-by-pictures given in the previous subsection. It is straightforward to derive the corresponding expression for the U-component of polarization (Exercise 10),

$$U(\hat{z}) = -A \int d\Omega_{n'} f(\hat{n}') \sin^2\theta' \sin(2\phi'). \tag{10.53}$$

The combination of sines here is proportional to $Y_{2,2} - Y_{2,-2}$. Again, only an incident quadrupole produces U polarization.

We can now relate the outgoing Q and U to the moments of the incident unpolarized distribution. We'll do this in four steps, in increasing generality.

- First, we'll consider the polariztion induced by a wavevector $\vec{k}$ in the $\hat{x}$-direction.
- Next, we allow $\vec{k}$ to lie anywhere in the $\hat{x}$-$\hat{z}$ plane.
- Then, we consider the most general possible wavevector.
- The first three steps will give us Q and U of the outgoing radiation along the z-axis. We need to generalize this to arbitrary outgoing directions.

The reason that we need to move so slowly is that the photon distribution, $f(\hat{n}')$, takes its cue from the direction of the wavevector. Recall that, in Chapter 4, we wrote the photon distribution as the sum of a zero-order piece — the uniform Planck distribution — and a perturbation, characterized by $\Theta(k, \mu)$ (e.g., Eq. (4.35)). There μ was the dot product of the wave vector $\hat{k}$ and the direction of propagation. Here we have labeled the direction of propagation of the incident photon as $\hat{n}'$, so $\mu = \hat{k} \cdot \hat{n}'$. Thus, $f(\hat{n}')$ in Eq. (10.52) will be an expansion in Legendre polynomials with argument $\hat{k} \cdot \hat{n}'$. This argument is *not* equal to the cosine of θ', since θ' is the angle between the external z-axis and $\hat{n}'$. Relating μ to θ' and ϕ' therefore is not trivial, and we will proceed slowly.

Let's first consider the wave vector $\vec{k}$ to lie in the $\hat{x}$-direction. Then,

$$\begin{aligned}\mu \equiv \hat{k} \cdot \hat{n'} &= \left(\hat{n'}\right)_x \\ &= \sin\theta' \cos\phi'. \end{aligned} \tag{10.54}$$

Recall that we decomposed the perturbation Θ into a sum over Legendre polynomials, so

$$\begin{aligned}\Theta(k, \hat{k} \cdot \hat{n'}) &= \sum_l (-i)^l (2l+1)\Theta_l(k)\mathcal{P}_l\left(\hat{k} \cdot \hat{n'}\right) \\ &\to -5\Theta_2(k)\mathcal{P}_2\left(\sin\theta' \cos\phi'\right), \end{aligned} \tag{10.55}$$

where the last line follows by substituting our expression for μ (Eq. (10.54)) and considering only the relevant quadrupole part of the sum.

A plane wave with wavevector $\vec{k}$ pointing in the $\hat{x}$-direction therefore has

$$Q(\hat{z}, \vec{k} \parallel \hat{x}) = 5A\Theta_2(k) \int_0^\pi d\theta' \sin\theta' \int_0^{2\pi} d\phi' \mathcal{P}_2\left(\sin\theta' \cos\phi'\right) \sin^2\theta' \cos 2\phi'. \tag{10.56}$$

Recall that $\mathcal{P}_2(\mu) = (3\mu^2 - 1)/2$. The $-1/2$ part of this gives no contribution to the integral since the ϕ' integral over $\cos(2\phi')$ vanishes. Therefore, we are left with

$$Q(\hat{z}, \vec{k} \parallel \hat{x}) = \frac{15A\Theta_2(k)}{2} \int_0^\pi d\theta' \sin^5\theta' \int_0^{2\pi} d\phi' \cos^2\phi' \cos 2\phi'. \tag{10.57}$$

The ϕ' integral is $\pi/2$, while the θ' integral — easily done by defining $\mu' = \cos\theta'$ — is $16/15$. So

$$Q(\hat{z}, \vec{k} \parallel \hat{x}) = 4\pi A\Theta_2(k). \tag{10.58}$$

We've now made part of the connection between polarization — represented by Q here — and the formalism of anisotropies — described by Θ in general and Θ_2 specifically for the quadrupole. This expression though applies only in the very simple case that the wavevector points along the x-axis, perpendicular to the line of sight.

Let's generalize this expression to wavevectors pointing in an arbitrary direction in the $\hat{x}$-$\hat{z}$ plane: $\hat{k} = (\sin\theta_k, 0, \cos\theta_k)$. In this case, the factor of $(\hat{k} \cdot \hat{n'})^2$ coming from $\mathcal{P}_2$ is $\sin^2\theta_k \sin^2\theta' \cos^2\phi' + \cos^2\theta_k \cos^2\theta'$. The first term is identical to the $\hat{k} \parallel \hat{x}$ case just derived, multiplied by $\sin^2\theta_k$. The second term introduces no new ϕ' dependence; since the integral over $\cos(2\phi')$ vanishes, it does not contribute. Therefore

$$Q(\hat{z}, \vec{k} \perp \hat{y}) = 4\pi A \sin^2\theta_k \Theta_2(k). \tag{10.59}$$

In Exercise 10 you will show that there is no U-polarization from this type ($\vec{k}$ in the $\hat{x}$-$\hat{z}$ plane): the polarization is all Q.

For any single plane wave, we can always rotate our coordinate system around the z-axis to ensure that the plane wave lies in the $\hat{x}$-$\hat{z}$ plane, so that Eq. (10.59)

applies. When we come to consider the real universe, however, with its superposition of many plane-wave perturbations, we won't have this luxury. Instead, we will need to account for the most general wavevector with orientation $\hat{k} = (\sin\theta_k \cos\phi_k, \sin\theta_k \sin\phi_k, \cos\theta_k)$. For this more general perturbation, you can go through (Exercise 9) exactly the same types of calculations as went into Eq. (10.59) to show that

$$Q(\vec{z}, \vec{k}) = 4\pi A \sin^2\theta_k \cos(2\phi_k)\Theta_2(k)$$

$$U(\vec{z}, \vec{k}) = 4\pi A \sin^2\theta_k \sin(2\phi_k)\Theta_2(k). \tag{10.60}$$

We must make one final generalization. Until now, we have focused solely on the outgoing radiation along the z-axis. Of course, not all outgoing rays will be along the z-axis. (This is what we are looking for: difference in polarization as a function of angle.) To account for arbitrary directions, we need to allow the polar angle θ_k in Eq. (10.60) to be the angle between the observation direction $\hat{n}$ and $\hat{k}$. So $\cos\theta_k \to \hat{n}\cdot\hat{k}$, and of course $\sin^2\theta_k$ becomes $1-(\hat{n}\cdot\hat{k})^2$. Therefore, for observations near the z-axis, the outgoing polarization induced by incoming unpolarized incident radiation is

$$Q(\hat{n}, \vec{k}) = 4\pi A\left[1 - \left(\hat{n}\cdot\hat{k}\right)^2\right]\cos(2\phi_k)\Theta_2(k)$$

$$U(\hat{n}, \vec{k}) = 4\pi A\left[1 - \left(\hat{n}\cdot\hat{k}\right)^2\right]\sin(2\phi_k)\Theta_2(k). \tag{10.61}$$

These expressions are valid only for directions $\hat{n}$ near the z-axis. This restriction is due to the dependence on the azimuthal angle, ϕ_k. Far from the z-axis, $\cos(2\phi_k)$ and $\sin(2\phi_k)$ give way to much more complicated expressions depending on both $\hat{n}$ and $\hat{k}$. Near the z-axis, though, the relatively simple sine and cosine describe the dependence on azimuthal angle. Thus, we will work in the small angle limit, where all observation directions are close to one another, clustered around the z-axis.

Equations (10.61) allow us to draw polarization patterns around the z-axis for arbitrary $\hat{k}$ modes. Consider the four patterns in Figure 10.16. In each case, the z-axis is out of the page in the center of the panel. For $\vec{k}$ in the $\hat{x}$-$\hat{y}$ plane ($\theta_k = 90°$), Eq. (10.61) says that the strength of the polarization as a function of $\hat{n}_x$ and $\hat{n}_y$ varies as

$$1 - (\hat{n}\cdot\hat{k})^2 = 1 - (\hat{n}_x\hat{k}_x + \hat{n}_y\hat{k}_y)^2. \tag{10.62}$$

That is, deviations from the maximum at $\hat{n}_x = \hat{n}_y = 0$ are small, quadratic in $\hat{n}_x, \hat{n}_y$. The orientation of the polarization in these cases can be either Q (top left panel, $\phi_k = 0$) or U (bottom left panel, $\phi_k = 45°$). For $\vec{k}$ out of the $\hat{x}$-$\hat{y}$ plane, we begin to observe changes in the polarization strength. The two right panels in Figure 10.16 illustrate these changes. Again there can be either Q or U polarization. The most important feature of these patterns is that the polarization strength is always changing in the direction parallel or perpendicular to the sense of the

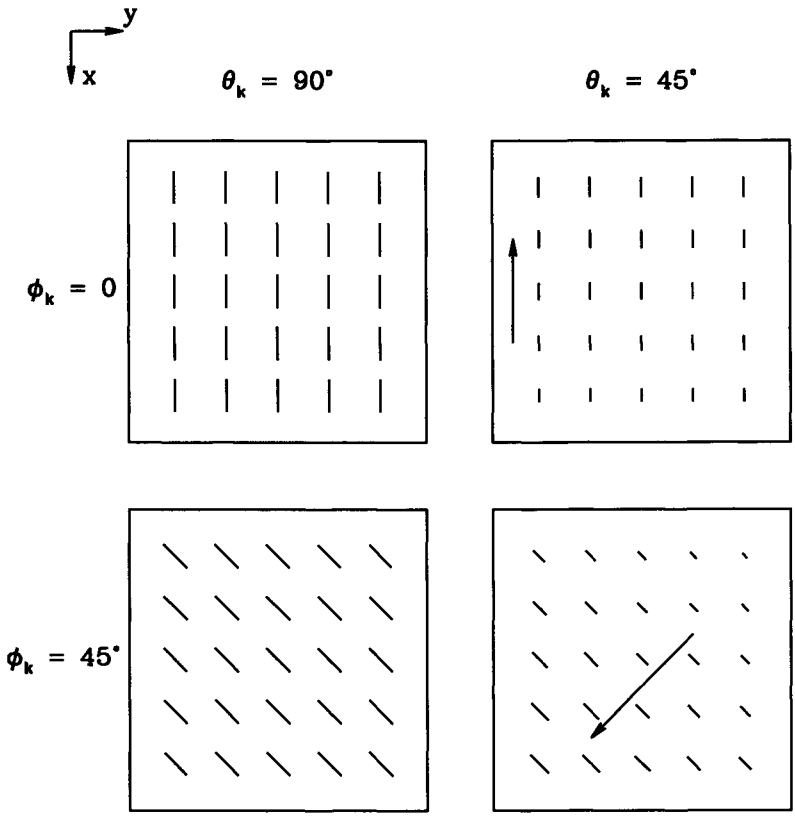

Figure 10.16. Polarization patterns near the z-axis arising from four plane wave perturbations with different $\vec{k}$. E.g., upper left arises from $\vec{k}$ along the x-axis ($\theta_k = 90°, \phi_k = 0$). For $\hat{k}$ in the $\hat{x}$-$\hat{y}$ plane (two left panels with $\theta_k = 90°$), polarization is at a maximum at $\hat{z}$, so little variation is seen. Arrows in right panel show direction in which polarization strength increases. This direction (or the direction perpendicular to it along which polarization remains constant) is aligned with the polarization pattern. This alignment is the hallmark of an E-mode.

polarization. In the top right panel, polarization is aligned with the x-axis, and this is the direction in which the polarization strength is changing. In the bottom right panel, polarization is aligned along $\hat{x}+\hat{y}$, and the change is along the perpendicular direction $\hat{x}-\hat{y}$. We will soon decompose polarization into E and B modes, just as we did the shear pattern in weak lensing. The patterns observed here are all pure E. Indeed, scalar perturbations generate only E modes.

We can also begin to understand the E/B decomposition. The polarization generated by scalar perturbations, the E mode, varies in strength in the same direction as its orientation. This conjures images of an electric field. An electric field from a point source, $\vec{E} = q\hat{r}/r^2$, varies in strength as one moves away from the point source. The electric field is pointed in the same direction: radially away

from the source. As one moves in the direction of the field, the strength of the field decreases. In Section 10.9, we will encounter the B mode, and see that—just like a magnetic field—the B mode of polarization varies in strength in a different direction from that in which it is pointing.

10.7 BOLTZMANN SOLUTION

To make quantitative predictions for the polarization expected in the CMB, we must go beyond the treatment of the previous section. There, we sat a single electron at the origin and considered the polarization emerging from incoming radiation with a given distribution. The real problem has lots of electrons coupled to an evolving photon distribution. For this, we need the Boltzmann equation. We wrote down the relevant equations in Chapter 4, although it will take a little bit of work to relate the variable we used there, Θ_P, to Q and U introduced above. The relevant equations ((4.101) and (4.102)) from Chapter 4 are

$$\dot{\Theta}_P + ik\mu\Theta_P = -\dot{\tau}\left[-\Theta_P + \frac{1}{2}\Big(1 - \mathcal{P}_2(\mu)\Big)\Pi\right] \tag{10.63}$$

$$\Pi = \Theta_2 + \Theta_{P2} + \Theta_{P0} \tag{10.64}$$

where $\mu \equiv \hat{k}\cdot\hat{n}$, and Θ_{P0} and Θ_{P2} are the monopole and quadrupole, respectively, of the polarization field.

We are left with the question of the relationship between Θ_P and Q, U. Θ_P is the strength of the polarization, while Q and U together describe both the strength and the orientation. In Chapter 4, we implicitly chose $\hat{k}$ to to lie in the $\hat{x}$-$\hat{z}$ plane in Chapter 4. In that case, we have just seen that the polarization is all Q, so

$$\begin{aligned} Q(\hat{z},\vec{k}) &= \Theta_P(\hat{z},\vec{k}) \\ U(\hat{z},\vec{k}) &= 0 \qquad\qquad \hat{k}\perp\hat{y}. \end{aligned} \tag{10.65}$$

More generally, for arbitrary $\vec{k}$, at least for directions $\hat{n}$ close to $\hat{z}$, we have

$$\begin{aligned} Q(\vec{k},\hat{n}) &= \Theta_P(\hat{k}\cdot\hat{n})\cos(2\phi_k) \\ U(\vec{k},\hat{n}) &= \Theta_P(\hat{k}\cdot\hat{n})\sin(2\phi_k). \end{aligned} \tag{10.66}$$

Equation (10.66) is a crucial connection between the polarization pattern $Q(\hat{n}), U(\hat{n})$ we are interested in and $\Theta_P(\mu \equiv \hat{k}\cdot\hat{n})$ for which we have Boltzmann equations. Now all we need to do is solve the Boltzmann equations for Θ_P, and then use Eq. (10.66) to construct power spectra for Q and U. We attack the first task in this section and the second in the next.

First, though, to solidify this connection between Θ_P and Q, U, it is instructive to rederive the result of the previous section for an incoming unpolarized wave

using the Boltzmann equation. We found there (Eq. (10.59)) that the outgoing polarization (for $\hat{k}$ in the $\hat{x}$-$\hat{z}$ plane) was proportional to $(1-\mu^2)\Theta_2$ where μ is the cosine of the angle between $\hat{k}$ and $\hat{z}$. Can we get this from the Boltzmann equation? In the absence of any prior polarization, Eq. (10.63) reduces to

$$\begin{aligned}\dot{\Theta}_P &= -\dot{\tau}\frac{1-\mathcal{P}_2(\mu)}{2}\Pi \\ &= \frac{-3\dot{\tau}}{2}(1-\mu^2)\Theta_2. \end{aligned} \tag{10.67}$$

Integrating over η, we find that the polarization induced by Compton scattering from incident unpolarized radiation is

$$\Theta_P = \frac{3\tau}{2}(1-\mu^2)\Theta_2, \tag{10.68}$$

i.e. the optical depth times the quadrupole modulated by the geometric factor $1-\mu^2$, in agreement with the less formal derivation advanced above. We also see that the strength of the polarization generated is proportional to the optical depth, τ, the integral along the line of sight of the free electron density times the Thomson cross-section.

Now let's solve the Boltzmann equation for the polarization. In analogy to Eq. (8.46), the formal solution to Eq. (10.63) for Θ_P is

$$\Theta_P(\hat{n},\vec{k}) = \int_0^{\eta_0} d\eta e^{i\vec{k}\cdot\hat{n}(\eta-\eta_0)-\tau(\eta)} S_P(k,\mu,\eta), \tag{10.69}$$

where the source term is

$$S_P(k,\mu,\eta) = -\frac{3}{4}\,\dot{\tau}\,\left(1-\mu^2\right)\,\Pi. \tag{10.70}$$

Remember that the visibility function is defined as $-\dot{\tau}e^{-\tau}$, so

$$\Theta_P(\hat{n},\vec{k}) = \frac{3}{4}\left(1-\mu^2\right)\int_0^{\eta_0} d\eta e^{i\vec{k}\cdot\hat{n}(\eta-\eta_0)} g(\eta)\Pi(k,\eta). \tag{10.71}$$

A reasonable approximation is to assume that we can evaluate the integrand — except for the rapidly changing visibility function — at the time of decoupling (for standard recombination). Then, since the visibility function integrates to unity,

$$\Theta_P(\hat{n},\vec{k}) \simeq \frac{3\Pi(k,\eta_*)}{4}\left(1-\mu^2\right)e^{i\vec{k}\cdot\hat{n}(\eta_*-\eta_0)}. \tag{10.72}$$

Neglecting η_* compared with η_0 and rewriting the factors of μ as derivatives leads to

$$\Theta_P(k,\mu) \simeq \frac{3\Pi(k,\eta_*)}{4}\left(1+\frac{\partial^2}{\partial(k\eta_0)^2}\right)e^{-ik\eta_0\mu}. \tag{10.73}$$

To get the moments Θ_{Pl}, we must multiply Eq. (10.73) by $\mathcal{P}_l(\mu)$ and integrate over all μ as in Eq. (4.99). This gives (Eq. (C.15))

$$\Theta_{Pl}(k) \simeq \frac{3\Pi(k,\eta_*)}{4}\left(1+\frac{\partial^2}{\partial(k\eta_0)^2}\right) j_l(k\eta_0). \tag{10.74}$$

The sum of the spherical Bessel function and its second derivative can be rewritten using the spherical Bessel equation (C.13) as

$$j_l + j_l'' = -\frac{2j_{l-1}}{k\eta_0} + \frac{2(l+1)}{(k\eta_0)^2} j_l + \frac{l(l+1)}{(k\eta_0)^2} j_l. \tag{10.75}$$

Of the three terms on the right, the last one dominates on small scales. To see this, remember that the spherical Bessel function peaks roughly at $k\eta_0 \sim l$. Physically, this means that anisotropy on an angular scale l is determined by perturbations with wavelength $k^{-1} \sim \eta_0/l$. For our order-of-magnitude estimate, this means that we can take $k\eta_0$ to be of order l in the three terms on the right-hand side. The first is then of order l^{-1}, the second of order l^{-1}, and the last of order $l^2/(k\eta_0)^2 \sim 1$: the last term dominates. Therefore,

$$\Theta_{Pl}(k) \simeq \frac{3\Pi(k,\eta_*)}{4}\frac{l^2}{(k\eta_0)^2} j_l(k\eta_0). \tag{10.76}$$

In the tight coupling limit, we can express Π in terms of the quadrupole, which in turn is related to the dipole. As you can show in Exercise 12, $\Pi = 5\Theta_2/2$. Therefore, the polarization moments today are

$$\Theta_{Pl}(k) \simeq \frac{15\Theta_2(k,\eta_*)}{8}\frac{l^2}{(k\eta_0)^2} j_l(k\eta_0). \tag{10.77}$$

We can go one step further by noting that — in the tightly coupled limit — the quadrupole is proportional to the dipole (Eq. (8.34)). Therefore,

$$\Theta_{Pl}(k) \simeq -\frac{5k\Theta_1(k,\eta_*)}{6\dot{\tau}(\eta_*)}\frac{l^2}{(k\eta_0)^2} j_l(k\eta_0). \tag{10.78}$$

Equation (10.78) is a final expression for the polarization moments today assuming the tightly coupled limit. Three features are worthy of note. First, and most important, the polarization spectrum is seen to be smaller than the anisotropy spectrum by a factor of order $k/\dot{\tau}$ at the time of decoupling. We will quantify this in the next section, but we now understand that it is a direct result of the twin facts that polarization is generated by a quadrupole moment and the quadrupole is suppressed in the early universe due to Compton scattering. Second, we expect there to be oscillations in the polarization power spectrum because $\Theta_{Pl} \propto \Theta_1$, which undergoes acoustic oscillations. More quantitatively, we expect the polarization oscillations, just like the dipole, to be out of phase with the monopole. The peaks and troughs in the temperature anisotropy spectrum, arising primarily

from oscillations in the monopole, should then be out of phase with the peaks and troughs in the polarization power spectrum. Finally, there is no analogue here to the integrated Sachs–Wolfe effect which impacts the temperature anisotropy spectrum. Polarization cannot be induced by photons moving through changing gravitational potentials. Therefore, the polarization spectrum today is in some senses a more pristine view of the early universe, uncontaminated by later developments.

10.8 POLARIZATION POWER SPECTRA

Equation (10.78) is an expression for the polarization moments from a single plane wave. In the real universe, we have not just one plane wave, but a superposition of many waves, all with differing amplitudes $\Theta_P(\vec{k}, \hat{n})$. The angular power spectrum from a superposition of plane waves follows from the identical calculation on the temperature anisotropies (Eq. (8.68)):

$$C_{P,l} = \frac{2}{\pi} \int_0^\infty dk\, k^2 \left|\Theta_{Pl}(k)\right|^2 . \tag{10.79}$$

For quite a while, cosmologists computed this power spectrum without reference to Q or U. In 1997, a flurry of papers appeared which derived the power spectra for Q and U. These exploited Eq. (10.66) or large-angle generalizations of it.

Based on our solution for the power spectra of the different components of shear in Section 10.4, we have a sense of what to expect for the power spectra of Q and U. Consider first Figure 10.17. In the small angle limit, Q for example is a function of the 2D vector $\vec{\theta}$, the projection of $\hat{n}$ onto the plane perpendicular to the $\hat{z}$ axis. Thus, we can Fourier transform Q just as we Fourier transformed the shear fields above; its transform will depend on $\vec{l}$, the vector conjugate to $\vec{\theta}$. Based on our experience with weak lensing, we expect the power spectrum of $\tilde{Q}$ to depend not only on the magnitude of $\vec{l}$ but also on its orientation. Looking back at Eq. (10.66), we will not be surprised to find that this power spectrum, $C_{QQ}(\vec{l})$ is proportional to $C_{P,l}$. The proportionality constant is $\cos^2(2\phi_l)$, where ϕ_l is the angle $\vec{l}$ makes with the x-axis. Thus, the factor of $\cos(2\phi_k)$ in Eq. (10.66) becomes $\cos(2\phi_l)$ when we sum over all $\vec{k}$. Similarly, the power spectrum of $\tilde{U}$ is $\sin^2(2\phi_l)C_{P,l}$.

Let's derive this connection between the power spectra of Q and U and that of Θ_P explicitly. We can write the Q polarization as a sum over all plane waves:

$$Q(\vec{\theta}) = \int \frac{d^3k}{(2\pi)^3} \Theta_P(\vec{\theta}, \vec{k}) \cos(2\phi_k) \tag{10.80}$$

The modulating factor $e^{i\vec{x}\cdot\vec{k}}$ is set to 1 here, since we observe from only one position, and we are calling that position $\vec{x} = 0$. To deal with the $\cos(2\phi_k)$ factor, first note that it is equal to $\cos^2\phi_k - \sin^2\phi_k$, or in terms of the Cartesian components of $\vec{k}$:

$$\cos(2\phi_k) = \frac{k_x^2 - k_y^2}{k_x^2 + k_y^2}. \tag{10.81}$$

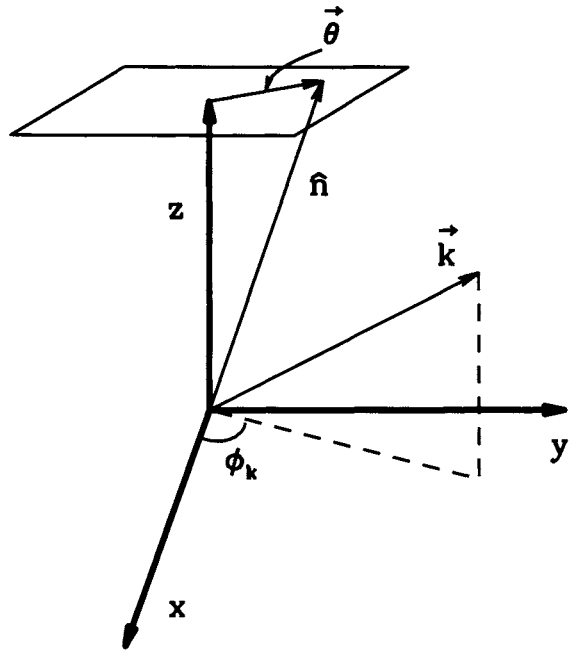

Figure 10.17. Different vectors in polarization. We observe radiation with incoming direction $\hat{n}$, also parameterized by 2D angle θ. Wavevector $\vec{k}$ has an azimuthal angle ϕ_k.

Since Θ_P has the exponential factor $e^{-i\vec{k}\cdot\hat{n}\eta_0}$ (e.g. Eq. (10.69)), and since $\hat{n}_x = \theta_x$ and $\hat{n}_y = \theta_y$, we can rewrite these Cartesian coordinates as derivatives with respect to the $\vec{\theta}$. For example, $k_x \to [-i\eta_0]^{-1}\partial/\partial\theta_x$. The full $\cos(2\phi_k)$ factor therefore can be written solely as derivatives with respect to $\vec{\theta}$:

$$\cos(2\phi_k) = D_Q(\vec{\theta}) \equiv \left[\frac{\partial^2}{\partial\theta_x^2} + \frac{\partial^2}{\partial\theta_y^2}\right]^{-1}\left(\frac{\partial^2}{\partial\theta_x^2} - \frac{\partial^2}{\partial\theta_y^2}\right). \tag{10.82}$$

This expression looks formidable, but it is extremely useful for summing up many different k-modes. We can replace Eq. (10.80) with

$$\begin{aligned} Q(\vec{\theta}) &= D_Q(\vec{\theta})\int \frac{d^3k}{(2\pi)^3}\Theta_P(\vec{\theta},\vec{k}) \\ &= D_Q(\vec{\theta})\Theta_P(\vec{\theta}). \end{aligned} \tag{10.83}$$

Both $Q(\vec{\theta})$ and $\Theta_P(\vec{\theta})$ can be written in terms of their Fourier transforms, so that Eq. (10.83) becomes

$$\int \frac{d^2l}{(2\pi)^2}e^{i\vec{l}\cdot\vec{\theta}}Q(\vec{l}) = D_Q(\vec{\theta})\int \frac{d^2l}{(2\pi)^2}e^{i\vec{l}\cdot\vec{\theta}}\Theta_{Pl}. \tag{10.84}$$

Now D_Q, which is so very complicated in θ-space, becomes very simple, for we know exactly what it looks like when it acts on the exponential $e^{i\vec{l}\cdot\vec{\theta}}$. In that case, it simply becomes $\cos(2\phi_l)$, where ϕ_l is the angle that the 2D vector $\vec{l}$ makes with the x-axis. Therefore, the Fourier transform of $Q(\vec{\theta})$ is

$$\tilde{Q}(\vec{l}) = \tilde{\Theta}_{Pl}\cos(2\phi_l). \tag{10.85}$$

An identical argument says that $U(\vec{l}) = \Theta_{Pl}\sin(2\phi_l)$. Therefore, the power spectra of $\tilde{Q}$ and $\tilde{U}$ are

$$\begin{aligned} C_{QQ}(\vec{l}) &= C_{P,l}\cos^2(2\phi_l) \\ C_{UU}(\vec{l}) &= C_{P,l}\sin^2(2\phi_l). \end{aligned} \tag{10.86}$$

Recall that in the case of weak lensing, we noticed that one could take linear combinations of γ_1 and γ_2 such that the power spectrum of one of the linear combinations vanishes (Eq. (10.40)), while the other is equal to the convergence power spectrum (Eq. (10.39)). Here we can do exactly the same thing. If we define

$$\begin{aligned} E(\vec{l}) &\equiv \tilde{Q}(\vec{l})\cos(2\phi_l) + \tilde{U}(\vec{l})\sin(2\phi_l) \\ B(\vec{l}) &\equiv -\tilde{Q}(\vec{l})\sin(2\phi_l) + \tilde{U}(\vec{l})\cos(2\phi_l) \end{aligned} \tag{10.87}$$

then

$$C_{BB}(\vec{l}) = 0. \tag{10.88}$$

In the small-scale limit, the power in the E-mode is precisely equal to C_P:

$$\lim_{l\gg 1} C_{EE}(\vec{l}) = C_{P,l}. \tag{10.89}$$

Figure 10.18 shows the resultant power spectrum, both the exact numerical result and the approximation of Eq. (10.78) integated over all modes as dictated by Eq. (10.79). Also shown is the spectrum of temperature anisotropies from Chapter 8. As expected it is higher in amplitude, since polarization is suppressed in the tightly coupled limit. Also as anticipated, the oscillations in the polarization spectrum are out of phase with those in the temperature spectrum. In 2002, the DASI experiment announced the first detection of polarization, a detection shown in Figure 10.18. This is akin to the first detection of shear by large scale structure, the beginning of our journey down promising new paths in cosmology.

The spectrum in Figure 10.18 is shown only on small scales; on larger scales, the treatment of this section needs to be modified (Kamionkowski, Kosowsky, and Stebbins, 1997a; Seljak and Zaldarriaga, 1997). The resultant spectrum has no surprises: it falls off very rapidly on large scales. Since the polarization is proportional to the dipole, which vanishes for large-scale modes, we could have anticipated this result as well. Although I won't go into the technical details of this large-angle

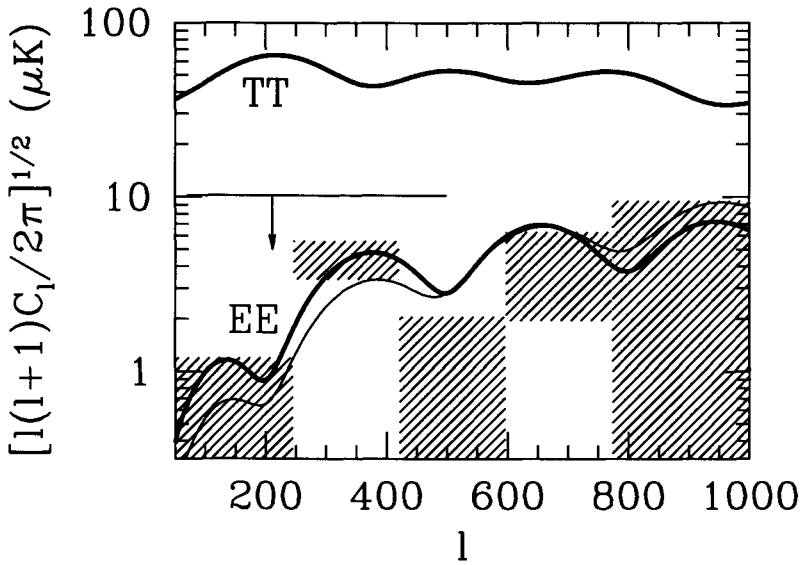

Figure 10.18. Power spectra of temperature and E-mode polarization for the standard CDM model. Thick curves show exact results; thin curve is the tight coupling approximation of Eq. (10.78). Only scalar perturbations have been assumed, so there is no power in the B-mode. Straight line at 10μK is an upper limit from Hedman *et al.*, 2002, while the hatched boxes are the first detection by the DASI experiment (Kovac *et al.*, 2002).

result, the basic idea is that instead of expanding polarization in terms of Legendre polynomials, or ordinary spherical harmonics, one must use tensor spherical harmonics.

One final comment: we have been implicitly assuming until now that the perturbations of interest are scalar. We inserted this assumption early on by writing the plane-wave perturbation as Eq. (10.55). If the perturbations were tensor, the decomposition would have included an azimuthal dependence; recall Eq. (4.115).

10.9 DETECTING GRAVITY WAVES

There is a fundamental difference between the scalar perturbations we have considered in the previous sections and tensor perturbations. A scalar plane-wave perturbation has one direction associated with it: the direction of the wavevector $\vec{k}$. Once this direction is specified, all photon moments depend only on the angle between the incoming photon and the wavevector. Once this angle is specified, there is an azimuthal symmetry about the $\hat{k}$ direction. This rotational symmetry is the reason that only the E mode is produced by scalar perturbations. There are two directions in a polarization field: (i) the direction in which the polarization strength is changing and (ii) the orientation of the polarization. For scalar perturbations, we saw in Figure 10.16 that these directions must be aligned (or perpendicular to each other).

Intuitively, each direction looks to the only vector it knows — $\vec{k}$ — for guidance, and they each arrive at the same end. This alignment is the salient characteristic of the E mode.

The photon distribution from tensor perturbations is not rotationally symmetric about the $\vec{k}$-direction. Gravity waves are pulsations in the metric; these induce an azimuthal dependence to the photon distribution. Recall from Eq. (4.115) that the resultant distribution varies as $\sin(2\phi)$ or $\cos(2\phi)$, where ϕ is the azimuthal angle about the $\vec{k}$-axis. This dependence on ϕ means that there is an additional direction to choose from when the polarization field gets induced. We might expect then that the orientation of the polarization will not necessarily be aligned with the direction of changing polarization strength. That is, we might expect that gravity waves will produce B-mode polarization. This is exactly what we will show in this section.

Before working through the algebra, we need to pause to understand the importance of the B-mode generated by tensor perturbations. Let's start with the difficulty of detecting tensors through the E-mode. Both scalars and tensors contribute to the E-mode, so the only way to disentangle them is to take advantage of differences in their spectra as a function of l. We saw in the case of temperature anisotropies that this is a tricky game, though, for other parameters can change spectra in ways similar to tensors. So even if we had perfect knowledge of the $C_{E,l}$ spectrum (no noise), we would still not necessarily know whether tensors were present. The B-mode is different. There is no contamination from scalar perturbations, so if we observe a B-mode in polarization, we know that it comes from gravity waves. In principle, this realization has unlimited power: no matter how small the tensor signal from inflation (no matter how small $H/m_{\rm Pl}$), we can ultimately detect this signal by searching for a B-mode. In practice, there are contaminants due to nonlinearities, but these are quite small. Estimates (Knox and Song, 2002; Kesden, Cooray, and Kamionkowski, 2002) suggest that the lowest obtainable limit on r, the tensor-to-scalar ratio, is of order 10^{-4}.

Let's compute the polarization pattern from a single plane wave generated by tensor perturbations. This problem is identical to that treated in Section 10.6. To find the outgoing polarization near the z-axis, we need to integrate over the incoming photon distribution. As in Eqs. (10.52) and (10.53), we want

$$\begin{aligned}\begin{pmatrix} Q \\ U \end{pmatrix} &\propto -\int d\Omega' \Theta^T(\Omega') \sin^2\theta' \begin{pmatrix} \cos(2\phi') \\ \sin(2\phi') \end{pmatrix} \\ &\propto -\int d\Omega' \Theta^T(\Omega') \begin{pmatrix} Y_{2,2}(\Omega') + Y_{2,-2}(\Omega') \\ \frac{1}{i}[Y_{2,2}(\Omega') - Y_{2,-2}(\Omega')] \end{pmatrix}, \end{aligned} \tag{10.90}$$

where I have inserted the photon distribution due to tensor perturbations, Θ^T; recognized the combination of $\sin^2\theta'$ and the azimuthal dependence as $Y_{2,2} \pm Y_{2,-2}$; and neglected the absolute normalization of the polarization.

To complete the calculation, we need to find the angular dependence of Θ^T. This is a bit more difficult than one might expect. Although we know that this angular dependence is $\sin^2\theta' \cos(2\phi')$ (for h_+) or $\sin^2\theta' \sin(2\phi')$ ($h_\times$) for $\vec{k}$ lying along the

z-axis, we need the dependence for a general wavevector $\vec{k}$. One way of finding this dependence is to rotate the coordinate system so that a unit vector pointing in the $\hat{z}$-direction gets rotated so that it points in the $\hat{k}$-direction. The relevant rotation matrix is

$$R = \begin{pmatrix} \cos\theta_k \cos\phi_k & -\sin\phi_k & \sin\theta_k \cos\phi_k \\ \cos\theta_k \sin\phi_k & \cos\phi_k & \sin\theta_k \sin\phi_k \\ -\sin\theta_k & 0 & \cos\theta_k \end{pmatrix}. \tag{10.91}$$

You should verify that R really does take $\hat{z} \to \hat{k}$ and work through a simple derivation of R (Exercise 13). We want to know what R does to Θ^T. To be concrete, let's focus on $h_\times$, so that $\Theta^T \propto \sin^2\theta' \sin(2\phi')$. First, we can reexpress this angular dependence in terms of the unit vector $\hat{n}'$ describing the direction of the incident photon:

$$\begin{aligned} \sin^2\theta' \sin(2\phi') &= 2\sin^2\theta' \sin\phi' \cos\phi' \\ &= 2\hat{n}'_x \hat{n}'_y. \end{aligned} \tag{10.92}$$

Now let's rotate the coordinate system so that the z-axis points in the direction of $\vec{k}$. The anisotropies due to the $h_\times$-mode used to be proportional to $\hat{n}'_x \hat{n}'_y$. In the new coordinate system, they become

$$\Theta^T \propto (R^t \hat{n}')_x (R^t \hat{n}')_y \tag{10.93}$$

where ^{t} denotes transpose.

Now we work through the matrix multiplication and find

$$\begin{aligned} \Theta^T &\propto (\cos\theta_k \cos\phi_k \sin\theta' \cos\phi' + \cos\theta_k \sin\phi_k \sin\theta' \sin\phi' - \sin\theta_k \cos\theta') \\ &\quad \times (-\sin\theta' \sin\phi_k \cos\phi' + \cos\phi_k \sin\theta' \sin\phi') \\ &= \sin\theta' \sin(\phi' - \phi_k) (\cos\theta_k \sin\theta' \cos(\phi' - \phi_k) - \sin\theta_k \cos\theta') \\ &= \frac{1}{2} \cos\theta_k \sin^2\theta' \sin[2(\phi' - \phi_k)] - \sin\theta' \cos\theta' \sin\theta_k \sin(\phi' - \phi_k). \end{aligned} \tag{10.94}$$

This last combination can be reexpressed in terms of spherical harmonics: it is a linear combination of $Y_{2,\pm2}, Y_{2,\pm1}$, and $Y_{2,0}$. That is, the anisotropy pattern about the wavevector $\vec{k}$ due to gravity waves (the $h_\times$ mode) has a $Y_{2,2} - Y_{2,-2}$ dependence when $\hat{k}$ is along the z-axis. When $\hat{k}$ is general, this dependence gets mixed up among all the $Y_{2,m}$'s. We are interested in the polarization pattern generated by Θ^T; from Eq. (10.90) and the orthogonality property of the spherical harmonics, this means we are interested only in the $Y_{2,\pm2}$ components of Θ^T. We can now extract these from Eq. (10.94). The last term on the right has a factor of $\sin(\phi' - \phi_k)$, so it is proportional to $Y_{2,\pm1}$, and we can neglect it. The first term is

$$\frac{1}{2} \cos\theta_k \sin^2\theta' \sin[2(\phi' - \phi_k)] = -\sqrt{\frac{32\pi}{15}} \frac{\cos\theta_k}{4i} \left[e^{-2i\phi_k} Y^*_{2,-2}(\Omega') - e^{2i\phi_k} Y^*_{2,2}(\Omega') \right]. \tag{10.95}$$

To find Q and U, we dot this into $Y_{2,2} \pm Y_{2,-2}$, so that the integral in Eq. (10.90) leads to

$$\begin{pmatrix} Q(\hat{z}) \\ U(\hat{z}) \end{pmatrix} \propto \Theta_0^T \cos\theta_k \begin{pmatrix} -\sin(2\phi_k) \\ \cos(2\phi_k) \end{pmatrix}. \tag{10.96}$$

If we move small angles away from the $\hat{z}$-direction, then the azimuthal dependence does not change, and $\cos\theta_k \to \hat{n} \cdot \hat{k}$, so that

$$\begin{pmatrix} Q(\hat{n}) \\ U(\hat{n}) \end{pmatrix} \propto \Theta_0^T \hat{n} \cdot \hat{k} \begin{pmatrix} -\sin(2\phi_k) \\ \cos(2\phi_k) \end{pmatrix}. \tag{10.97}$$

The polarization pattern described by Eq. (10.97) has a nonzero B-mode. To see this, first consider the definition of B in Eq. (10.87). This definition is in Fourier space, but we remember that using the operator $D_{Q,U}$, we can replace $\vec{l}$ with $\vec{k}$, the wavevector. Therefore, for $\vec{k}$ in the $\hat{x}$-$\hat{z}$ plane ($\phi_k = 0$), the B-mode corresponds to only U polarization. Indeed this is precisely what Eq. (10.97) says is produced by the $h_\times$ mode of gravity waves. So the anisotropies due to gravity waves do produce the B-mode of polarization.

Figure 10.19 shows the polarization patterns due to a single plane wave $h_\times \propto e^{i\vec{k}\cdot\vec{x}}$ for four different wavevectors $\vec{k}$. For example, the top left panel considers $\vec{k}$ lying along the x-axis. In that case, since $\phi_k = 0$, Eq. (10.97) says that the polarization is all U and that the strength scales as

$$\hat{n} \cdot \hat{k} = \hat{n}_x. \tag{10.98}$$

The strength of the polarization therefore increases as one moves away from the y-axis. The important feature of this pattern, which characterizes the B-mode, is that the strength of the polarization varies in the $\hat{x}$-direction, while the orientation is in the $\hat{x} \pm \hat{y}$ direction. These two directions (varying strength and polarization orientation) are *not* aligned or perpendicular to each other. The other panels show the same feature.

Figure 10.20 shows the anisotropy spectrum in a standard CDM model with an equal amount of tensors and scalars. The T and E spectra are similar to the tensorless case depicted in Figure 10.18. With tensors, the B spectrum is now nonzero, albeit small. Studies suggest that polarization searches will help significantly in the quest to detect small r.

SUGGESTED READING

Gravitational lensing is described in exquisite detail in *Gravitational Lenses* (Schneider, Ehlers, and Falco). An excellent, comprehensive review of weak lensing is in Bartelmann and Schneider (2001). Electromagnetic polarization is a textbook subject, covered in, for example, *Classical Electrodynamics* (Jackson) and *Radiative Processes in Astrophysics* (Rybicki and Lightman). Initial papers on gravitational lensing by large scale structure include Blandford *et al.* (1991), Miralda-Escude

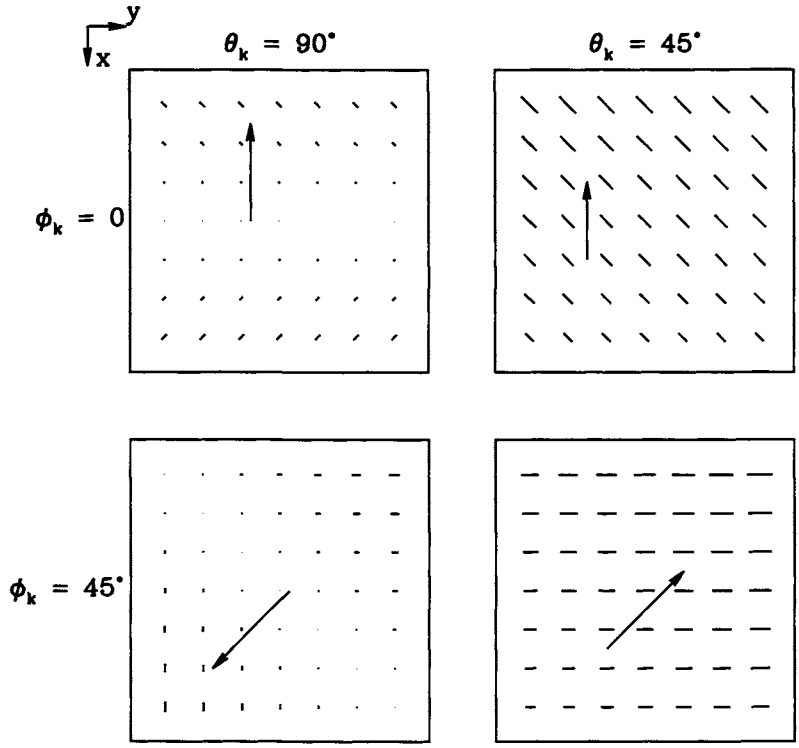

Figure 10.19. Polarization patterns from a single plane wave $h_\times(\vec{k})$ in a plane perpendicular to the z-axis ($\hat{z}$ out of the paper). Patterns from four different $\vec{k}$ are shown. Arrows depict direction of increasing polarization strength. This direction is *not* aligned with the orientation of the polarization.

(1991), and Kaiser (1992). Recent theoretical work connecting lensing observations to cosmological parameters includes Jain and Seljak (1997); Bernardeau, van Waerbecke, and Mellier (1997); and Hu and Tegmark (1999). The onset of the new millenium saw the first detections of lensing by large scale structure in van Waerbecke *et al.* (2000); Wittman *et al.* (2000); Bacon, Refrgier, and Ellis (2000); Kaiser, Wilson and Luppino (2000); and Maoli *et al.* (2001). Active work continues. The future will undoubtedly bring observations of weak lensing on large fields. Two proposal for such observations are the SuperNova Acceleration Probe (SNAP; `http://snap.lbl.gov`), which presently plans to devote $\sim 20\%$ of its time to weak lensing, and the Large Scale Synaptic Telescope (LSST; `http://www.dmtelescope.org`).

Polarization of the CMB was studied in the seminal papers of the 1980s by Bond and Efstathiou (1984) and Polnarev (1985). Kosowsky's thesis (1996) is a lucid Boltzmann-esque discussion of this work. The first papers to recognize the importance of the E/B decomposition were Stebbins (1996); Seljak (1997);

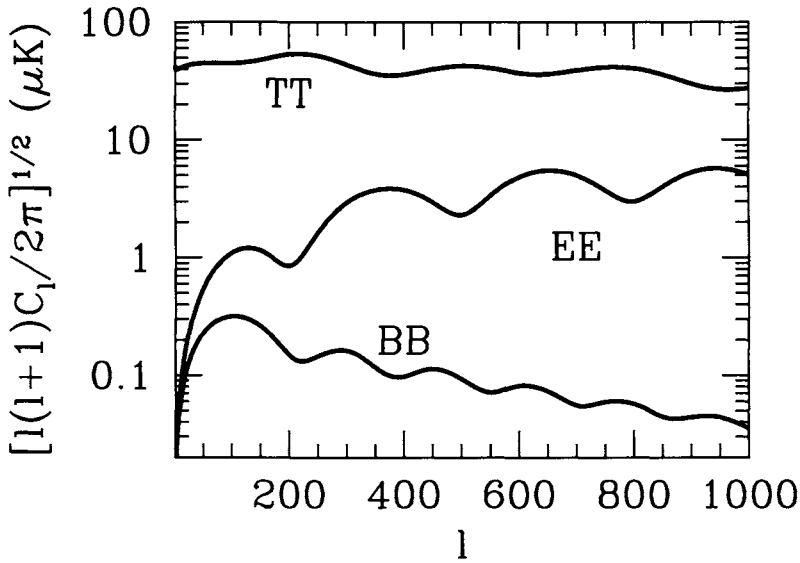

Figure 10.20. Anisotropy spectrum from a standard CDM model with equal amounts of scalar and tensor perturbations ($r = 1$). The T and E spectra come from both scalars and tensors, whereas the B-mode is due solely to tensors.

Kamionkowski, Kosowsky, and Stebbins (1997a,b), and Zaldarriaga and Seljak (1997). I've followed the treatment of Seljak who worked in the small angle limit because the algebra is simpler. The review article of Hu and White (1997b) is perhaps the most accessible introduction into the recent literature on polarization of the CMB, but it is a difficult subject. Even this lucid review with its illuminating pictures requires a lot of effort to understand.

DASI (Kovac *et al.*, 2002) detected polarization at the 5-sigma level. Previous stringent upper limits, which are still valuable on large scales, were obtained by Hedman *et al.* (2000) and Keating *et al.* (2001).

EXERCISES

Exercise 1. The probability that there will be a galaxy massive enough to act as a lens between a quasar at redshift z and us is roughly proportional to the volume between us. Compute

$$V(z) \equiv \int_{x<\chi(z)} d^3x. \tag{10.99}$$

The integral is trivial, but the dependence on z is not. Numerically compute $V(z)$ in a flat universe with cosmological constant. Plot $V(z)$ vs Ω_Λ for $z = 2, 3, 4$. If the galaxy density does not depend on cosmology, then the expected number of lenses scales simply as this volume. For $z = 3$, what is the ratio of lenses expected in a flat universe with $\Omega_\Lambda = 0.7$ as compared with a flat, matter-dominated universe?

Be warned that Keeton (2002), among others, has made a strong case that the expected lensing frequency does *not* vary this dramatically with cosmology because of differences in the galaxy densities in the different models.

Exercise 2. Compute the magnification of an image in terms of the convergence κ and shear γ_1 and γ_2. Show that, in the limit of weak fields, the magnification μ is related to the convergence via

$$\mu \simeq 1 + 2\kappa. \tag{10.100}$$

Exercise 3. It is often useful to write observable properties of lenses — such as deflection angles and shear — in terms of a *projected potential* ϕ.
(a) Using Eq. (10.14), determine the ϕ such that $\vec{\theta}_S = \vec{\theta} + \nabla\phi$ where ∇ is the gradient with respect to the 2D angular variable $\vec{\theta}$.
(b) Express the transformation matrix defined in Eq. (10.15) in terms of the projected potential.

Exercise 4. When the lens is at a fixed redshift (e.g., a single galaxy or a cluster as opposed to large-scale structure in general) z_L corresponding to comoving distance χ_L from us, show that the projected potential ϕ from the previous problem reduces to

$$\phi(\vec{\theta}; z_L) = 4G\frac{\chi_S - \chi_L}{\chi_S\chi_L}\int d^2R\Sigma(\vec{R}) \ln\left|\vec{R} - \chi_L\vec{\theta}\right|. \tag{10.101}$$

Here χ_S is the comoving distance out to the source; $\vec{R}$ is the radius in the plane perpendicular to the line of sight; and $\Sigma(\vec{R})$ is the projected surface density in this plane.

Exercise 5. Compute the observed component of ellipticity ϵ_2 from an intrinsically circular source; express it in terms of the components of the transformation matrix, κ, γ_1, and, most importantly, γ_2.

Exercise 6. **(a)** Show that the power spectrum of the convergence is given by Eq. (10.35). Show that the power spectrum of γ_2 is given by Eq. (10.36).
(b) Using CMBFAST or the BBKS transfer function, compute numerically P_κ for standard CDM with $\Omega_m = 1, h = 0.5, n = 1$. Assume all background galaxies are at redshift $z = 1$. At what l do you expect your result — based on the linear power spectrum — to lose validity due to nonlinear effects?

Exercise 7. Equation (10.34) gives the power spectrum of the convergence in the small angle limit ($l \gg 1$). The more general expression is (Stebbins, 1996, the extra factor of $(2\pi)^3$ here due to differing power spectrum conventions)

$$C_{\kappa,l} = 4\pi l^2(l+1)^2 \int \frac{d^3k}{(2\pi)^3}\, k^2 I_l^2(k\chi) P_\Phi(k) \tag{10.102}$$

when all background galaxies are at comoving distance χ and

$$I_l(x) \equiv \int_0^1 \frac{dy}{y}(1-y)j_l(xy). \tag{10.103}$$

(a) Verify, either analytically or numerically, that in the small-angle limit Eq. (10.102) reduces to the expression for $P_\kappa(l)$ in Eq. (10.34).
(b) Redo the calculation of the convergence power spectrum for the sCDM model of Exercise 6, this time using the general expression in Eq. (10.102).

Exercise 8. In the text, we computed the angular correlations of galaxies (Chapter 9) and the weak lensing correlation function (this chapter). One can also compute the cross-correlation, which measures how correlated the galaxies are with the mass. One way to measure this is to separate a galaxy sample into foreground and background galaxies and measure the cross-correlation between the two samples. Since they are separated by such large distances, the only possible correlation arises because the background galaxies have been magnified by the foreground mass. This problem allows you to work out the background/foreground correlation function (e.g., Moessner and Jain, 1998). Incidentally, this cross-correlation function can also be measured by the QSO/galaxy correlation function. Suppose the 2D overdensity of foreground galaxies is due solely to intrinsic inhomogenities, so that it is given by Eq. (9.3). Assume that the 2D overdensity of background galaxies arises only from magnification. That is, galaxies that should not be included in the survey because they are intrinsically fainter than the magnitude limit are magnified and so appear brighter, thereby making the cut. If the magnification is μ, then the number of background galaxies in an angular patch is

$$n_b = \bar{n}_b \mu^{2.5s-1}. \tag{10.104}$$

Here $\bar{n}_b$ is the average number of background galaxies, and s is defined as $d\log N(m)/dm$ where $N(m)$ is the number of galaxies at the magnitude limit m. For the present problem, don't worry about where this relation comes from (see Broadhurst, Taylor, and Peacock, 1995, for an explanation).
(a) Express δ_b, the background overdensity, in terms of κ and s using Eq. (10.100).
(b) Find an expression for the convergence $\kappa(\vec{\theta})$ in terms of the mass overdensity. First express it in terms of the relevant components of transformation matrix A of Eq. (10.17), but then eliminate the potential there in favor of the density field δ.
(c) Using these two expressions — Eq. (9.3) and your answer in **(b)** — for the foreground and background overdensities, compute the angular cross-correlation function $w_{bg}(\theta) \equiv \langle \delta_b(\theta)\delta_g(0)\rangle$.

Exercise 9. As the wavevector $\vec{k}$ moves out of the $\hat{x}$-$\hat{z}$ plane, show that the Q-polarization (for outgoing radiation in the $\hat{z}$-direction) changes as $\cos(2\phi_k)$. To do this, first compute $\hat{k}\cdot\hat{n}'$, and then integrate $\mathcal{P}_2(\hat{k}\cdot\hat{n}')$ over solid angle, with the weighting factor $\sin^2\theta'\cos(2\phi')$ derived in Eq. (10.52).

Exercise 10. This problem focuses on the U-component of polarization.
(a) We showed that the Q-component of polarization from unpolarized incident radiation is given by Eq. (10.52), which stems from Eq. (10.50). The Q-component thus depends on the difference between $|\hat{\epsilon}_i \cdot \hat{x}|^2$ and $|\hat{\epsilon}_i \cdot \hat{y}|^2$. For the U-component, $\hat{x}$ and $\hat{y}$ must be replaced by unit vectors rotated 45°, i.e., $(\hat{x}+\hat{y})/\sqrt{2}$ and $(\hat{x}-\hat{y})/\sqrt{2}$. With this replacement, derive Eq. (10.53).
(b) Show that a plane-wave perturbation with wavevector $\vec{k}$ lying in the $\hat{x}$-$\hat{z}$ plane does not produce any U-polarization in the outgoing $\hat{z}$-direction.
(c) For the most general orientation of the wavevector, $\hat{k} = (\sin\theta\cos\phi, \sin\theta\sin\phi, \cos\theta)$, show that U-polarization is given by Eq. (10.60).

Exercise 11. Draw the polarization patterns near the z-axis arising from a plane-wave scalar perturbation with (a) $\theta_k = \pi/8, \phi_k = \pi/8$; (b) $\theta_k = 3\pi/4, \phi_k = \pi/4$; (c) $\theta_k = 3\pi/4, \phi_k = 0$; and (d) $\theta_k = 3\pi/2, \phi_k = 0$. In each case, show that the sense of polarization is aligned with (or perpendicular to) the direction in which the polarization strength is changing.

Exercise 12. In the tight coupling limit, find an expression for $\Pi \equiv \Theta_2 + \Theta_{P2} + \Theta_{P0}$.
(a) When $\dot{\tau}$ is very large, the terms multiplying it on the right hand side of Eq. (10.63) must cancel. Write down this equality for $\Theta_P(\mu)$ in terms of the moments, Θ_2, Θ_{P2}, and Θ_{P0}.
(b) Expand $\Theta_P(\mu)$ in terms of Legendre polynomials, keeping only the monopole and the quadupole. Then equate the coefficients of $\mathcal{P}_0$ and $\mathcal{P}_2$.
(c) This leads to two equations for three unknowns. Show that solving for the two polarization moments in terms of the temperature quadrupole gives $\Theta_{P0} = 5\Theta_2/4$ and $\Theta_{P2} = \Theta_2/4$.
(d) Use the results of (c) to determine Π in terms of Θ_2.

Exercise 13. This problem concerns the rotation matrix R given in Eq. (10.91).
(a) Act with R on the unit vector $(0, 0, 1)$ and show that it gets transformed into $\hat{k}$.
(b) Derive R. One way to do this is to first rotate the x-y-z frame about the z-axis by an angle ϕ'. Then, rotate about the y-axis by an angle $-\theta'$. The product of these two rotations is R.

Exercise 14. In the text we considered polarization patterns from a single plane-wave perturbation due to gravity waves. There are actually two such orientations. We considered only $h_\times$. In this problem, consider polarization from h_+. In a frame in which $\hat{k}$ is along the z-axis the anisotropies have a $\sin^2\theta\cos(2\phi)$ dependence.
(a) Find the dependence of Θ^T on angle in the more general frame in which $\hat{k}$ does not lie along the z-axis.
(b) Determine Q and U from this incoming distribution.

(c) Plot the anisotropy pattern near the outgoing $\hat{z}$-direction for the four sets of θ_k, ϕ_k shown in Figure 10.19.

Exercise 15. Find expressions for the cross-correlation spectra between the temperature anisotropy and polarization anisotropy $C_{TQ}(\vec{l})$ and $C_{TU}(\vec{l})$ in terms of Θ_l and Θ_{Pl}. Assume scalar perturbations only. Express $C_{TE,l}$ in terms of these.

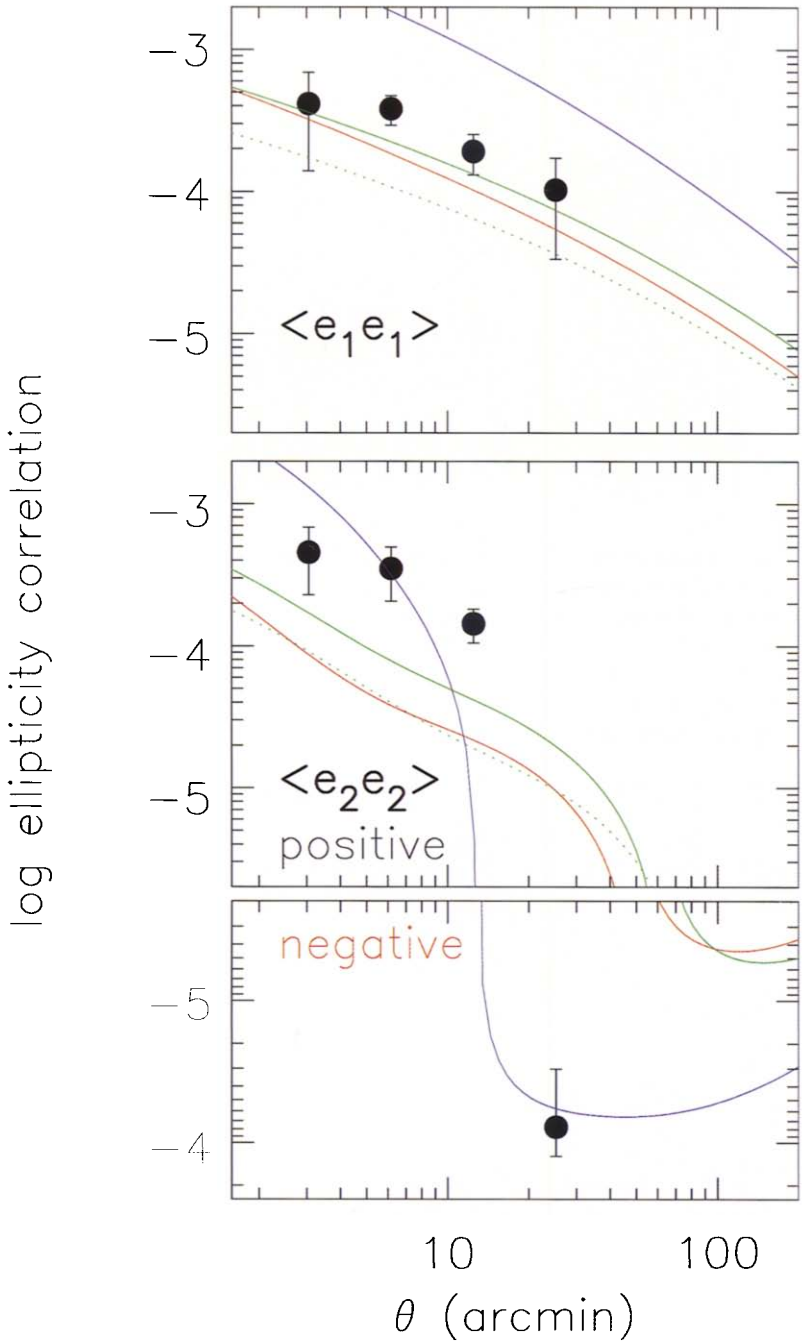

Plate 10.10. Measurement of the shear correlation functions using 145,000 background galaxies (Wittman *et al.*, 2000). Also shown are a variety of CDM models; topmost in top panel is standard CDM, ruled out here at many sigma. Note that $w_{\gamma_1} = \langle e_1 e_1 \rangle$ remains positive on all angular scales.

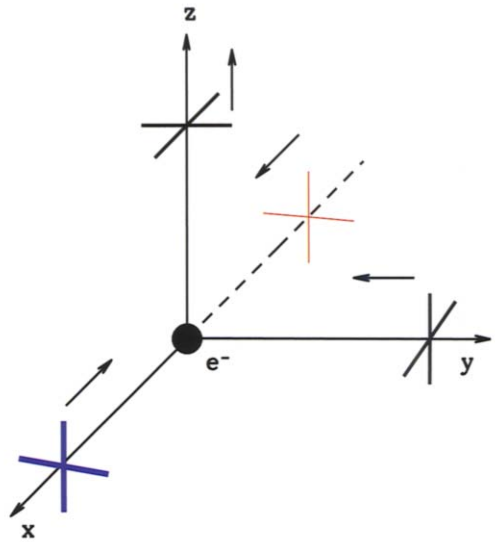

Plate 10.13. Incoming dipole radiation also produces no polarization. Heavy (thin) lines denote hot (cold) spots. Here the incoming radiation is hotter than average (average is medium thickness) from the $+\hat{x}$-direction, and colder than average from the $-\hat{x}$-direction. The two rays from the $\pm\hat{x}$-directions therefore produce the average intensity for the outgoing ray along the $\hat{y}$-direction. The outgoing intensity along the $\hat{x}$-direction is produced by the ray incident from the $\pm\hat{y}$-directions. Since these have the average intensity, the outgoing intensity is also the average along the $\hat{x}$-direction. The net result is outgoing unpolarized light.

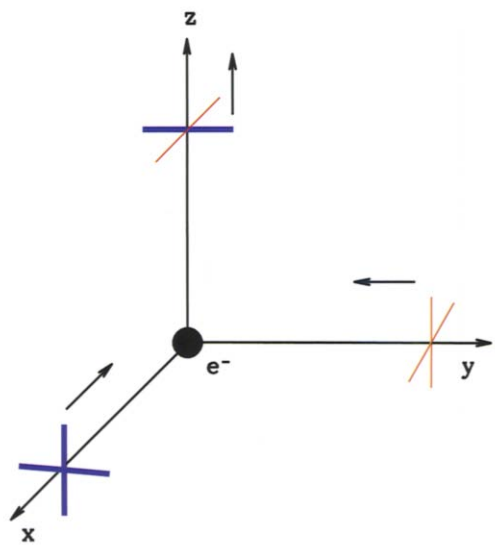

Plate 10.14. Incoming quadrupole radiation produces outgoing polarized light. The outgoing radiation has greater intensity along the y-axis than in the $\hat{x}$-direction. This is a direct result of the hotter radiation incident from the $\hat{x}$-direction.